Journal of Medicinal Chemistry

pubs.acs.org/jmc

Article

Overcoming Paradoxical Kinase Priming by a Novel MNK1 Inhibitor

Elisabeth Bou-Petit,[#] Stefan Hümmer,*[,#] Helena Alarcon, Konstantin Slobodnyuk, Marta Cano-Galietero, Pedro Fuentes, Pedro J. Guijarro, María José Muñoz, Leticia Suarez-Cabrera, Anna Santamaria, Roger Estrada-Tejedor, José I. Borrell,* and Santiago Ramón y Cajal*

Cite This: *J. Med. Chem.* 2022, 65, 6070−6087

Read Online

ACCESS | Metrics & More | Article Recommendations | Supporting Information

ABSTRACT: Targeting the kinases MNK1 and MNK2 has emerged as a valuable strategy in oncology. However, most of the advanced inhibitors are acting in an adenosine triphosphate (ATP)-competitive mode, precluding the evaluation of different binding modes in preclinical settings. Using rational design, we identified and validated the 4,6-diaryl-pyrazolo[3,4-*b*]pyridin-3-amine scaffold as the core for MNK inhibitors. Signaling pathway analysis confirmed a direct effect of the hit compound **EB1** on MNKs, and in line with the reported function of these kinases, **EB1** only affects the growth of tumor but not normal cells. Molecular modeling revealed the binding of **EB1** to the inactive conformation of MNK1 and the interaction with the specific DFD motif. This novel mode of action appears to be superior to the ATP-competitive inhibitors, which render the protein in a pseudo-active state. Overcoming this paradoxical activation of MNKs by **EB1** represents therefore a promising starting point for the development of a novel generation of MNK inhibitors.

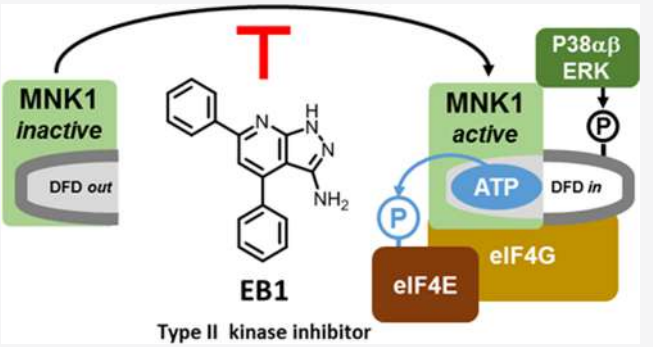

INTRODUCTION

Altered regulation of mRNA translation is a frequent feature of cancer. Cell signaling pathways regulating mRNA translation are in many cancers not only affected by genetic alterations but also by the tumor environment, and aberrant mRNA translation is therefore a widespread characteristic of tumor cells.[1,2] Consequently, therapeutic targeting of the protein synthesis apparatus is emerging as a valuable strategy in oncology.

A key player in the regulation of cap-dependent mRNA translation is the eukaryotic translation initiation complex 4F (eIF4F), and eIF4E is the rate-limiting component of this complex.[3] Many studies over the last years have revealed that deregulation of eIF4E is implicated in tumorigenesis and cancer progression.[4,5] In line with this, we and others have described eIF4E as an independent prognostic factor in several tumors.[1]

The MAP kinase interacting kinases (MNK1/2) execute a unique function in regulating eIF4E through phosphorylation at the conserved residue Ser 209. This phosphorylation of eIF4E is necessary for oncogenic transformation but appears to be dispensable for normal development.[6] Furthermore, MNKs phosphorylation of eIF4E has been shown to be involved in tumor metastasis.[7−9] The increased requirement for MNK-dependent phosphorylation of eIF4E with malignancy is thought to selectively upregulate the translation of certain mRNAs involved in tumor cell survival and dissemination.[4] With the implementation of cancer immunotherapy into the clinics, the previously described immune-regulatory functions of MNKs have also regained attention in the field of oncology. Those functions may either be achieved through the regulation of cytokine signaling and response[10,11] or even directly through the regulation of immune checkpoint proteins like PD-L1 in tumor cells. Importantly, MNK inhibition in this context has been shown to have a major impact on tumor development and metastasis.[12−14]

In the tumor environment, cancer cells are exposed to various stresses, including hypoxia and immune responses as well as treatment-induced alterations in hormone levels or DNA damage. In response to those alterations, activation of MNKs can be achieved through the MAPK stress response pathways (ERK and p38α/β) and promote cellular survival.[1,15] In this context, experiments with cell lines from breast and pancreatic cancer as well as with glioblastoma revealed that phosphorylation of eIF4E is required for survival from genotoxic stress, caused by DNA damaging agents.[16−18] Furthermore, resistance to hormone deprivation therapies in breast and prostate cancers has been linked to elevated levels

Received: November 12, 2021
Published: April 13, 2022

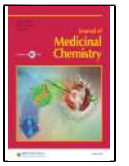

https://doi.org/10.1021/acs.jmedchem.1c01941
J. Med. Chem. 2022, 65, 6070−6087

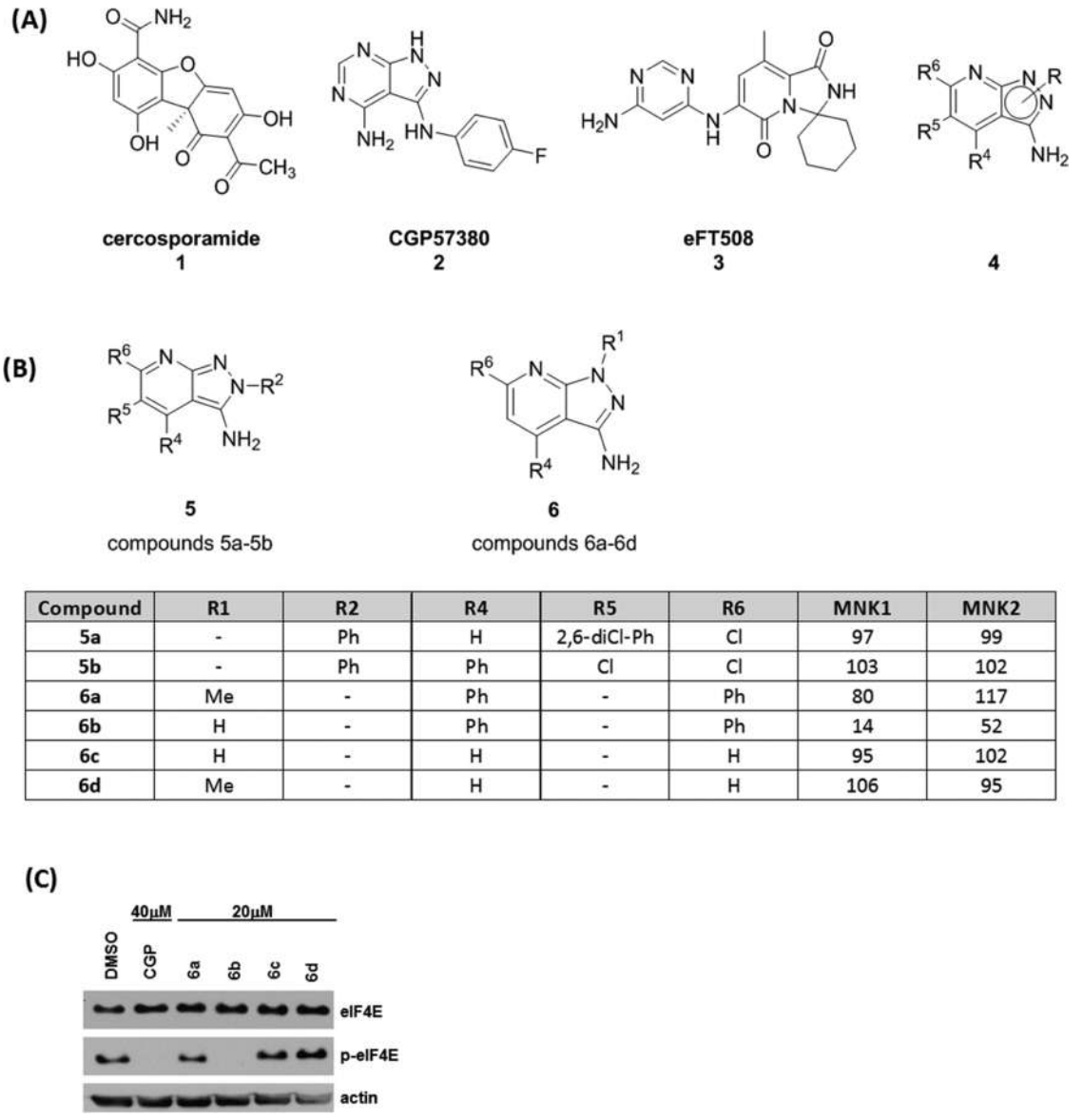

Compound	R1	R2	R4	R5	R6	MNK1	MNK2
5a	-	Ph	H	2,6-diCl-Ph	Cl	97	99
5b	-	Ph	Ph	Cl	Cl	103	102
6a	Me	-	Ph	-	Ph	80	117
6b	H	-	Ph	-	Ph	14	52
6c	H	-	H	-	H	95	102
6d	Me	-	H	-	H	106	95

Figure 1. Study of the pyrazolo[3,4-*b*]pyridin-3-amine scaffold as an MNK inhibitor. (A) Structure of the pyrazolo[3,4-*b*]pyridin-3-amine scaffold (**4**) and the known inhibitors used as references (**1**, **2**, **3**). (B) Inhibitory activity of pyrazolo[3,4-*b*]pyridine derivatives. Results from the enzymatic radiometric assay. Values indicated as residual activity of kinases MNK1 and MNK2 after treatment with the indicated compounds at 10 μM. (C) Western blot analysis of MDA-MB-231 cells treated with pyrazolo[3,4-*b*]pyridine derivatives for 24 h. Dimethyl sulfoxide (DMSO) and CGP (CGP57380) are used as negative and positive controls, respectively.

of p-eIF4E and MNK inhibition has been shown to increase the sensitivity to those treatments.[19,20]

MNKs belong to the family of Ser/Thr kinases, are classified as members of Ca^{2+}/calmodulin-dependent kinases, and are present in two isoforms: MNK1 and MNK2.[21,22] The catalytic domains of MNKs, while being overall conserved to other protein kinases, contain three unusual elements: two short sequence insertions and a DFD instead of the classical DFG-motif.[23,24] These elements provide the base for an MNK specific regulatory mechanism, in which the kinase activity is autoinhibited by conversion of the activation segment into an autoinhibitory module.[24] Although this regulatory mechanism accounts for both kinases, the autoinhibition is more stringent in the case of MNK1, while MNK2 possesses higher constitutive basal activity. While both kinases can be activated by ERK, only MNK1 contains a shared docking motif for p38α/β and ERK, which allows its activation by both kinases.[25]

Although several investigational compounds have been used over the last years for the study of MNKs function, agents such as cercosporamide (**1**)[26] and CGP57380 (**2**)[27] (Figure 1A) also inhibit several other protein kinases with similar or greater potency compared to MNKs.[28,29] Effort has been therefore devoted to the identification of novel selective MNK inhibitors. In recent years, compounds like eFT508 (**3**),[30] BAY1143269,[31] SEL-201,[7] ETC-206,[32] MNK-I1,[9] and the MNK-I1-derived MNK2 selective inhibitor MNK-7g[33] have been developed and tested in preclinical settings. Among those, currently, eFT508, BAY1143269, and ETC-206 are tested in clinical trials in oncology.[13,34] Notably, all of those inhibitors, even though having a different chemical scaffold, are categorized as Type I inhibitors, acting in an adenosine triphosphate (ATP)-competitive manner on the active conformation of the kinase.[29] Studies on inhibitors of other protein kinases have however revealed that some Type I kinase

https://doi.org/10.1021/acs.jmedchem.1c01941
J. Med. Chem. 2022, 65, 6070−6087

(A)

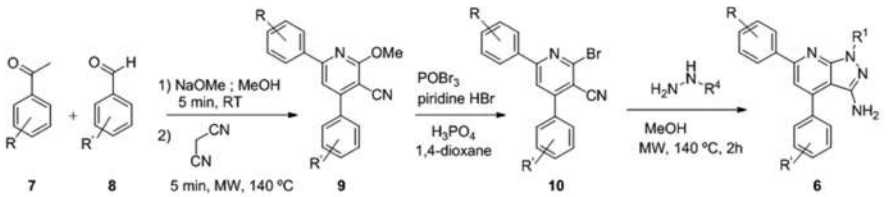

(B)

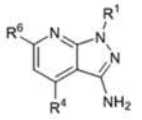

6

compounds 6b-6o

Compound	R6	R4	R1	MNK1	MNK2
cercosporamide (1)	-	-	-	0	1
6b	Ph	Ph	H	14	52
6e	*p*-MeO-Ph	*p*-MeO-Ph	H	60	101
6f	*p*-MeO-Ph	*p*-Me-Ph	H	45	82
6g	*m*-MeO-Ph	Ph	H	38	74
6h	*o*-MeO-Ph	*p*-MeO-Ph	H	63	109
6i	*o*-MeO-Ph	*p*-Me-Ph	H	61	123
6j	*m*-MeO-Ph	*p*-F-Ph	H	51	82
6k	Ph	*p*-MeO-Ph	H	25	74
6l	*m*-MeO-Ph	*p*-MeO-Ph	H	41	92
6m	*p*-MeO-Ph	*p*-MeO-Ph	Me	94	154
6n	Ph	*p*-MeO-Ph	Me	102	145
6o	Ph	*p*-F-Ph	H	31	62

(C)

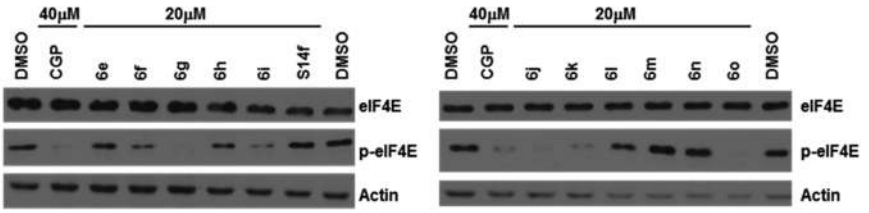

Figure 2. Study of the 4,6-diaryl pyrazolo[3,4-*b*]pyridin-3-amines as MNK inhibitors. (A) General synthesis of 4,6-diaryl pyrazolo[3,4-*b*]pyridin-3-amine derivatives. (B) Inhibitory activity of 4,6-diaryl pyrazolo[3,4-*b*]pyridin-3-amine derivatives. Results from the enzymatic radiometric assay. Values indicated as residual activity of kinases MNK1 and MNK2 after treatment with the indicated compounds at 10 μM. Cercosporamide is used as a positive control. (C) Western blot analysis of MDA-MB-231 cells treated with the indicated concentrations of the 4,6-diaryl pyrazolo[3,4-*b*]pyridin-3-amine derivatives for 24 h. DMSO and CGP (CGP57380) are used as negative and positive controls, respectively.

inhibitors are prone to activate noncatalytic functions of the target protein.[35−37] For the clinical translation of the mainly genetic-based proposal of targeting MNKs as a promising new strategy in oncology, it is therefore desirable to identify non-ATP-competitive inhibitors to evaluate different modes of kinase inhibition in preclinical and clinical settings.

RESULTS AND DISCUSSION

Identification of New Scaffolds as MNK Inhibitors. In recent years, the development of new MNK inhibitors has been centered on small synthetic structures. Among those, bicyclic nitrogenated compounds appear to be a privileged scaffold for the inhibition of these kinases. Here, we propose the use of the pyrazolo[3,4-*b*]pyridin-3-amine core (**4**) (Figure 1A) as a new alternative scaffold as an MNK inhibitor. Detailed analysis of CGP57380 (**2**) indicated that the pyridine- and pyridone-based scaffolds could be an alternative to the widely reported pyrimidine-based structures as the 5-N is not involved in the direct interaction of the molecule with the ATP binding site.[38] In addition, work by Yu et al. suggested that the 3-amino group of this part of the molecule would form an additional interaction with Phe227 in the ATP binding pocket of MNK2.[39]

To study the suitability of new scaffolds, several families of compounds were prepared and the inhibition of MNK1 and

https://doi.org/10.1021/acs.jmedchem.1c01941
J. Med. Chem. 2022, 65, 6070−6087

(A)

Compound	IC50 MNK1 [μM]	IC50 MNK2 [μM]
CGP (2)	1,52	6,27
EB1	0,69	9,4
EB2	4,2	22
EB3	1,3	4,1

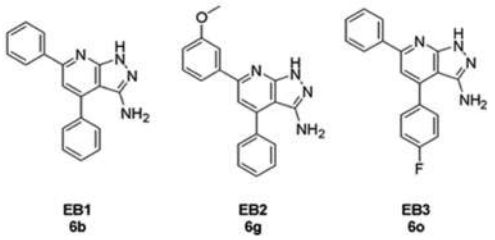

(B)

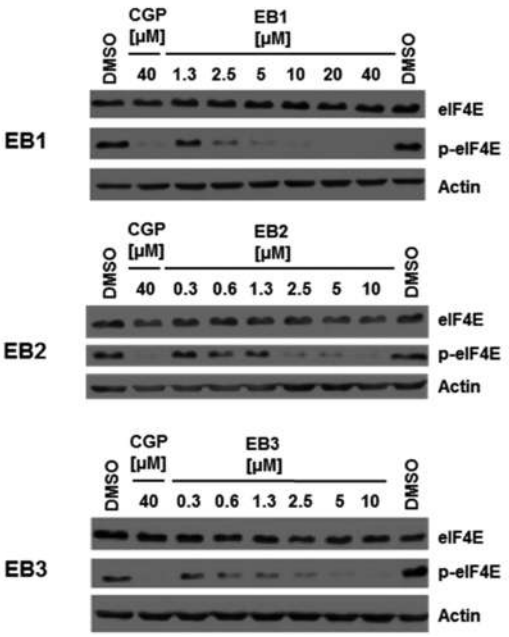

Figure 3. 4,6-Diaryl pyrazolo[3,4-*b*]pyridin-3-amines compounds as MNK inhibitors. (A) IC_{50} values obtained for the selected 4,6-diaryl pyrazolo[3,4-*b*]pyridin-3-amine derivatives. CGP (CGP57380) is used as a positive control. (B) Titration curves of the selected 4,6-diaryl pyrazolo[3,4-*b*]pyridin-3-amine derivatives in MDA-MB-231 cells. DMSO and CGP (CGP57380) are used as negative and positive controls, respectively. Cells were treated for 24 h with the inhibitors, and western bot analysis with the indicated antibodies was carried out.

MNK2 kinase activity was tested with a radiometric protein kinase assay ([33]PanQinase Activity Assay, Reaction Biology).

The first stage of the study (see the Supporting Information) was focused on exploring the suitability of 3-amino-pyrazolo-[3,4-*b*]pyridin-6-one scaffold (**S11**, Figure S1A). These structures were obtained by the cyclization of 2-methoxy-6-oxo-1,4,5,6-tetrahydropyridin-3-carbonitriles (**S13**), synthesized by the reaction of an *α*,*β*-unsaturated ester (**S12**) and malononitrile in NaOMe/MeOH, with hydrazine or substituted hydrazines (Figure S1B).[40] We synthesized 37 compounds with a broad combination of substituents in the most interesting points of this scaffold (R2, R4, and R5). The compounds under study combined bulky and small substituents in the pyridone ring (H, Me, Ph, and substituted aromatic rings) and in the pyrazole ring (H, Me, Ph, substituted Ph and acyl groups) to explore the maximum number of possibilities (compounds **S14a−g**, **S15a−x**, and **S16a−f**). However, none of the newly developed molecules was able to inhibit MNK1/2 kinase activity *in vitro* (Figure S2).

Next, we included a set of modifications of the original scaffold by oxidizing and methylating the lactam ring (compounds **S17a−c**, **S18a−d**, and **S19**) (Figure S1C), substituting the pyrazole ring in the N1 position[41] and testing the importance of the NH_2 group[42] (compounds **S20** to **S25**). The set of 14 new compounds prepared did not show any significant activity in the kinase assay *in vitro* (Figure S3). Therefore, the pyrazolo[3,4-*b*]pyridin-6-one scaffold did not appear suitable for the development of new MNK kinase inhibitors.

While the lactam ring is a central feature of several kinase inhibitors and was proposed to have a positive effect on the potency and selectivity of MNK inhibitors,[43−46] none of our synthesized compounds was able to inhibit MNKs kinase activity (Figures S2 and S3). Therefore, we focused next on molecules containing a pyridine ring instead of the pyridone ring to increase aromaticity and to obtain a more planar structure (**4**, Figure 1A). A new set of compounds **5a−b** and **6a−d** with a pyrazolo[3,4-*b*]pyridin-3-amine core was synthesized. Modifications included: (a) aromatization of the lactam ring by capturing the enolic form of the lactam with a halogenating agent forming a 6-chloropyridine ring and (b) inclusion of substituents of different bulkiness (H, Me, Ph) at positions R1/R2, R4, and R6. Among those compounds, **6b** was able to inhibit the MNK1 and MNK2 kinase activity *in vitro* (Figure 1B).

Having identified a biochemically active compound, we next tested its activity in a cell-based assay. Since phosphorylation of eIF4E at S209 is uniquely carried out by MNK kinases, the assessment of p-eIF4E by western blot analysis directly reflects

https://doi.org/10.1021/acs.jmedchem.1c01941
J. Med. Chem. 2022, 65, 6070−6087

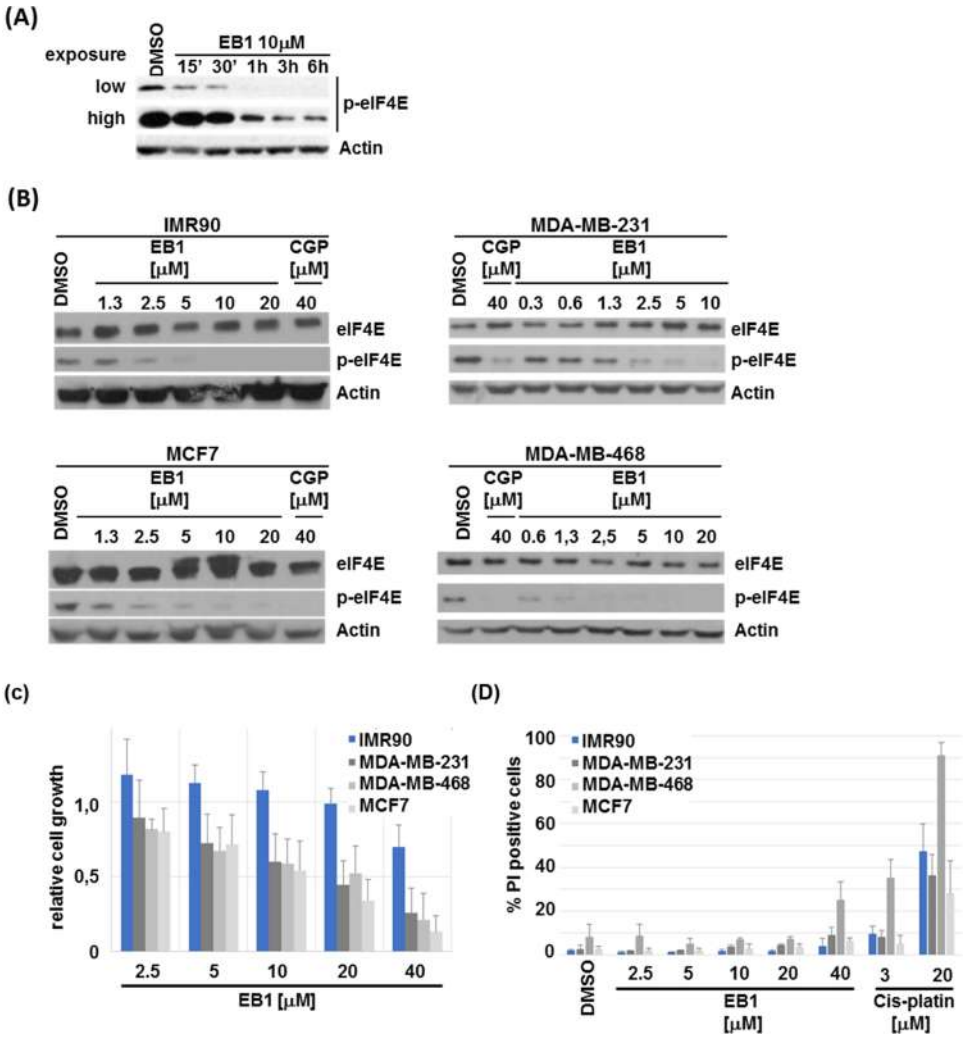

Figure 4. Characterization of **EB1**. (A) Analysis of the inhibition of eIF4E phosphorylation in MDA-MB-231 cells treated with 10 μM **EB1** for the indicated times. (B) Titration curve of **EB1** in the cell lines MDA-MB-231, MDA-MB-468, MCF7, and IMR90. Treatment was carried out for 72 h, and inhibition of eIF4E phosphorylation was analyzed by western blotting with the indicated antibodies. (C) Effect of **EB1** on cell growth in the same cell lines as in (B). Cells were treated for 72 h with the indicated concentrations of **EB1** and cell growth was analyzed by crystal violet staining. The GI_{50} values are 15.08 (+/- 1.2) μM (MDA-MB-231), 14.46 (+/- 1.2) μM (MDA-MB-468), 8.46 (+/- 1.1) μM (MCF7), and >40 μM for IMR90. (D) Cytotoxicity of **EB1** on different cell lines. Cells were treated as described in (C), Hoechst and Propidium iodide (PI) was added to the cell culture medium, and the fraction of PI-positive cells was determined microscopically. *Cis*-platin and DMSO are used as positive and negative controls, respectively. Error bars represent the standard deviation of three independent experiments.

MNK1/2 activity. Treatment of MDA-MB-231 cells with compounds bearing a pyrazolo[3,4-*b*]pyridin-3-amine core revealed that only **6b** resulted in a clear inhibition of eIF4E phosphorylation (Figure 1C). The structure−activity relationship (SAR) analysis of these results revealed two requirements for the activity of the first hit compound: (1) the presence of the two phenyl rings at the C4 and C6 positions of the pyrazolo[3,4-*b*]pyridine scaffold and (2) the absence of substituents (methyl) at the pyrazole ring.

In summary, out of the nearly 60 synthesized and tested compounds, we identified **6b** as a first hit compound, which was able to inhibit the kinase activity of MNK1/2 *in vitro* and eIF4E phosphorylation in cells.

4,6-Diaryl-pyrazolo[3,4-*b*]pyridin-3-amine scaffold as a Core for MNK Inhibitors. To confirm the activity of the core structure and to test the effect of substituents on the biological activity, we generated derivatives of **6b**. A family of 4,6-diphenyl-1*H*-pyrazolo[3,4-*b*]pyridin-3-amines was designed with different substituents in both phenyl rings and in the pyrazole ring, and a total of 11 derivatives of **6b** (**6e−o**) were synthesized. The synthesis starts by the condensation of the corresponding substituted acetophenone (**7**) with the appropriate substituted benzaldehyde (**8**) in NaOMe/MeOH at room temperature followed by the Michael addition with malononitrile under microwave irradiation to afford upon cyclization of the Michael intermediate the corresponding cyanomethoxypyridine (**9**). The conversion of the methoxy group of **9** into a better leaving group is achieved upon treatment with $POBr_3$ in 1,4-dioxane in the presence of Pyridine·HBr to yield the bromo-substituted pyridine (**10**). Finally, the cyclization with the appropriate hydrazine in MeOH affords the corresponding pyrazole[3,4-*b*]pyridines **6e−o** (Figure 2A). Test for their inhibitory effect on MNK1 and MNK2 kinase assay revealed that several derivatives were able to inhibit the kinase activity of MNKs. Remarkably, the more active compounds in the *in vitro* kinase assays were also able to inhibit p-eIF4E phosphorylation in MDA-MB-231 cells, highlighting the biological activity of this new compound

https://doi.org/10.1021/acs.jmedchem.1c01941
J. Med. Chem. 2022, 65, 6070−6087

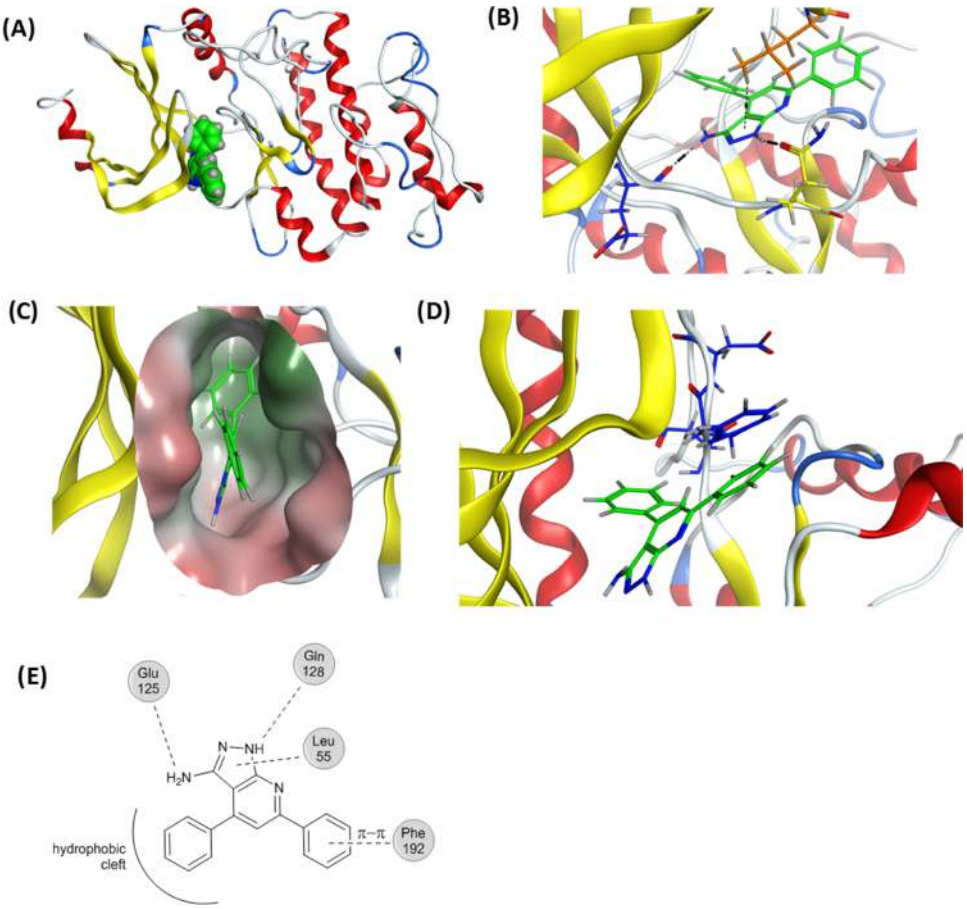

Figure 5. Computational study of the binding mode of **EB1** to MNK1. (A) Model of **EB1** (green) bound to the inactive conformation of MNK1. (B) Interactions formed between the 3-aminopyrazole ring of **EB1** (green) and residues Glu125 (blue), Gln128 (yellow), and Leu55 (orange). (C) Surface representation of the pocket. The phenyl ring in position C4 of **EB1** (green) fits the inner hydrophobic part of the pocket. (D) $\pi-\pi$ stacking between the Phenyl ring in position C6 of **EB1** (green) and Phe 192 (blue). The interaction is maintained during the whole simulation. Image taken after 36 ns of simulation. (E) Summary of the interactions of **EB1** with the inactive conformation of MNK1.

family of MNK inhibitors (Figure 2B,C). Therefore, the 4,6-diaryl-1*H*-pyrazolo[3,4-*b*]pyridin-3-amine represents a new core structure for MNK1/2 inhibitors with biological activity.

SAR analysis revealed that the aromatic and planar structure of the pyrazolo[3,4-*b*]pyridine system is essential for biological activity. This is in particular exemplified by the initial compounds presenting a pyrazolo[3,4-*b*]pyridin-6-one scaffold (Figures S2 and S3, compounds **S14a–g**, **S15a–x**, **S16a–f**, **S17a–c**, **S18a–d**, and **S19**), which did not present any MNK1/2 inhibitory activity despite containing equivalent substituents. In line with the results obtained above (Figure 1B,C), the lack of activity of compound **6c** indicates that the C4 and C6 phenyl rings are essential substituents of the pyrazolo[3,4-*b*]pyridine-3-amine core structure, to achieve inhibitory activity on MNK1/2. Moreover, the substitution of the pyrazole ring scaffold appears to render the compounds inactive as shown in Figures 1B,C and 2B,C. The drop in the activity of the methyl-substituted compounds **6a**, **6m**, and **6n** in comparison with the corresponding unsubstituted compounds **6b**, **6e**, and **6k** supports this. Therefore, the presence of an unsubstituted pyrazole moiety is a structural requirement of 4,6-diphenyl-1*H*-pyrazolo[3,4-*b*]pyridin-3-amines as inhibitors of MNK1 and MNK2, indicating that the presence of a H-bond donor in such a ring is essential for the activity of these scaffolds. Supporting this further, all compounds presenting the unsubstituted pyrazole ring showed inhibition of at least one of the MNK kinases.

In summary, we have identified and validated 4,6-diaryl-1*H*-pyrazolo[3,4-*b*]pyridin-3-amines as a novel core structure for MNK1/2 inhibitors and **6b**, the more potent compound of this family, was chosen for further detailed analysis.

Characterization of the EB Family of Compounds. We finally selected the compounds **6b**, **6g**, and **6o**, from now on named **EB1**, **EB2**, and **EB3**, respectively, for quantitative analysis and determined their IC_{50} for MNK1 and MNK2 in protein kinase assays. As summarized in Figure 3A, all three compounds inhibited MNK1 and MNK2 activity and displayed a 4- to 14-fold lower IC_{50} for MNK1. The first hit compound **EB1** was maintained as the more active and selective MNK1 inhibitor with an IC_{50} of 0.69 μM for MNK1 compared to an IC_{50} of 9.4 μM for MNK2. Moreover, treatment of MDA-MB-231 cells revealed a dose-dependent inhibition of MNK activity as judged by the reduction of eIF4E phosphorylation (Figure 3B).

In summary, the 4,6-diphenyl-1*H*-pyrazolo[3,4-*b*]pyridin-3-amine-based compounds **EB1**, **EB2**, and **EB3** represent a new class of biologically active MNK1/2 inhibitors with a higher affinity for MNK1 compared to MNK2.

Characterization of EB1. Focusing on **EB1**, we next carried out a detailed characterization of its biological activity. To exclude cell-line-specific effects of **EB1** activity, we assessed

https://doi.org/10.1021/acs.jmedchem.1c01941
J. Med. Chem. 2022, 65, 6070–6087

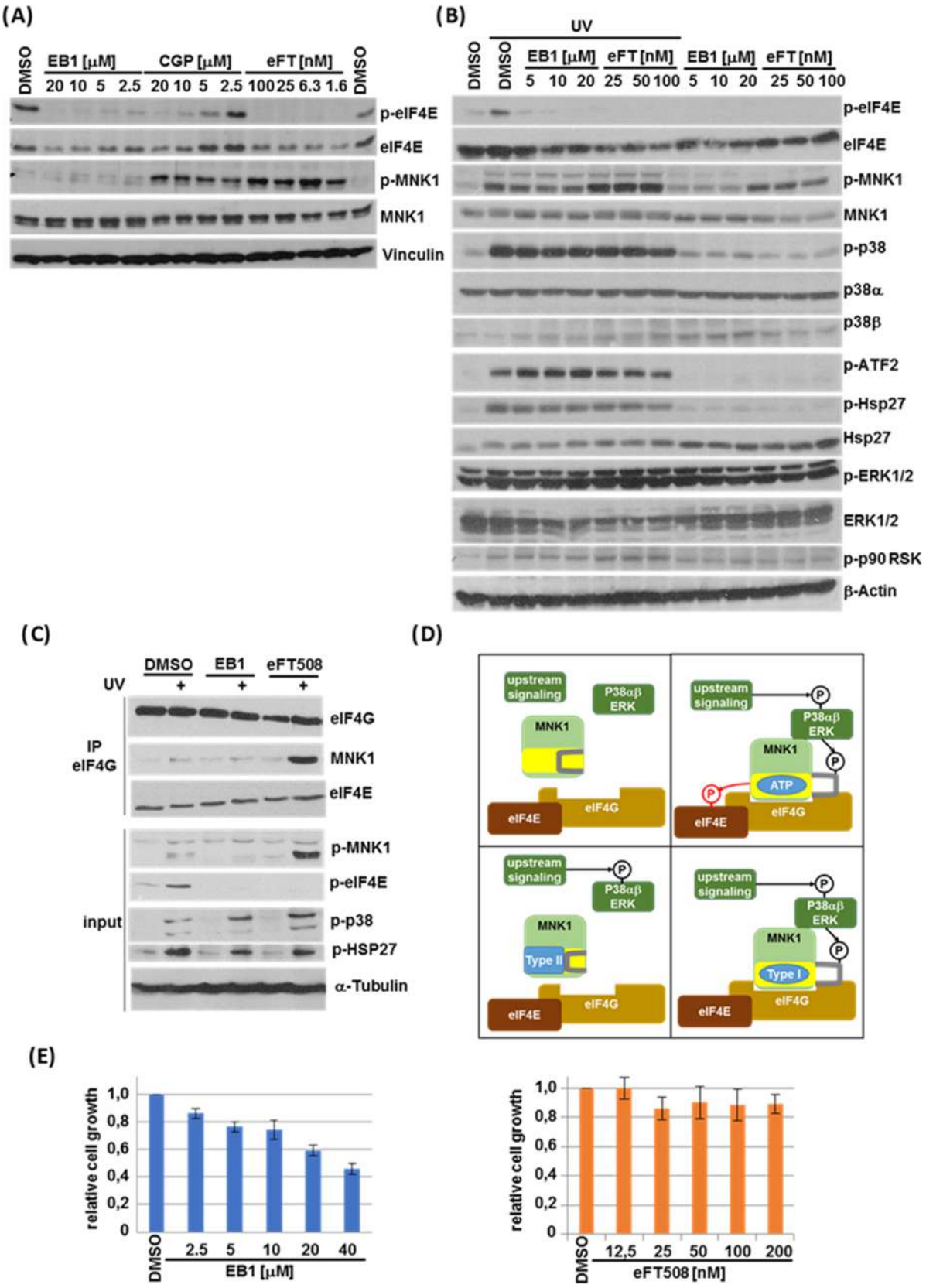

Figure 6. Comparison of **EB1** to Type-I MNK inhibitors. (A) Western blot analysis of MDA-MB-231 cells treated for 24 h with the indicated concentrations of **EB1**, eFT508 (eFT), and CGP57380 (CGP). (B) Treatment of MDA-MB-231 cells with the indicated concentrations of **EB1**, eFT508 (eFT), and CGP57380 (CGP) for 24 h followed by treatment with UV irradiation and recovery for 40 min. Western blot analysis was carried out with the indicated antibodies. (C) Immunoprecipitation of endogenous eIF4G from cell extracts of HEK-293 cells treated for 24 h with DMSO, 20 μM **EB1**, or 100 nM eFT508 followed by UV irradiation and recovery for 40 min. Western blot analysis of Immunoprecipitate (IP) and total cell extracts (input) are shown. (D) Schematic drawing indicating the activity status of MNK1 and the MNK1−eIF4G interaction. Proteins

https://doi.org/10.1021/acs.jmedchem.1c01941
J. Med. Chem. 2022, 65, 6070−6087

Figure 6. continued

are described in the figure. Phosphorylation events are indicated by -P. The activation loop of MNK1 is depicted in gray, and active MNK is indicated by bound ATP. Top left: inactive MNK1 is not bound to eIF4G; top right: activation of MNK1 by upstream kinase signaling and binding to eIF4G; bottom left: Type-II inhibitor binding maintains MNK1 in the inactive conformation and MNK1 does not bind to eIF4G; bottom right: Type-I inhibitor binding renters MNK1 into the active conformation allows phosphorylation by upstream kinases and binding to eIF4G. (E) MDA-MB-231 cells treated for 72 h with the indicated concentrations of **EB1** and eFT508. Cell growth was determined by crystal violet staining. Error bars represent the standard deviation of three independent experiments.

the inhibition of eIF4E phosphorylation in other cell lines of solid tumors like MDA-MB-468 and MCF7 (breast cancer), 22RV1 (prostate cancer), A375M (melanoma), as well as in the leukemia cell line (MV4-11) (Figures 4 and S4). In line with the results described above for MDA-MB-231 (Figure 3B), treatment of cells for 24 h with **EB1** also resulted in a dose-dependent inhibition of eIF4E phosphorylation in all other cell lines tested, which therefore excludes cell-line-specific effects of **EB1**.

Next, we studied the dynamics of **EB1** inhibition in MDA-MB-231 cells. Time course experiments revealed a fast inhibition of MNK activity (<30 min) (Figure 4A). Moreover, this inhibition was maintained in long-term treatments (>72 h), arguing for the stability of the compound under physiological conditions (Figure 4B).

To study the phenotypic consequences of MNK inhibition by **EB1**, we focused on cell growth. Previous studies in MEFs obtained from the MNK1/2 knock-out mice have revealed that the function of those kinases is not required for normal cell growth.[47] In contrast, various studies have reported the requirement for phosphorylation of eIF4E by MNKs for tumor cell growth *in vitro* and *in vivo*.[48−51] To test for drug selectivity, we therefore used fibroblast (IMR90) and breast cancer cell lines (MDA-MB-231, MDA-MB-468, and MCF7) as models for normal and transformed cells, respectively, and analyzed cell growth after the treatment with **EB1**. As shown in Figure 4C, cell growth was not affected in IMR90 cells up to 20 μM and only a slight but not significant effect could be observed at higher concentrations. In contrast, a dose-dependent inhibition of cell growth could be observed in all tested breast cancer cell lines (Figure 4C). Propidium iodide (PI) staining carried out in parallel did not reveal a significant increase in the number of dead cells in all tested cell lines compared to the cytotoxic agent cis-platin (Figure 4D). FACS analysis in MDA-MB-231 cells (Figure S5) could finally confirm these results, as in contrast to the positive control doxorubicin, an increase in the proportion of "sub G1" cells was not detected in **EB1**-treated cells.

In summary, analysis of cell growth and cell death did not reveal adverse effects of **EB1** in the noncancerous cell line IMR90 but caused a reduction of cell growth in breast cancer cell lines. This is in line with the requirement on MNKs for the growth of cancer cells but not of normal cells. This also supports the selectivity of the compound in a cellular context, as an unperturbed cell growth in the presence of **EB1** (up to 20 μM) precludes significant targeting of any cellular protein required for this.

EB1 Represents a Novel Type of MNK Inhibitor. To determine the mode of action of **EB1**, we employed molecular docking in combination with molecular dynamics (MD) to study the binding mode of **EB1** to the active and inactive conformations of MNK1. Based on the available crystal structures of MNK1 (PDB ID: 2HW6) and MNK2 (PDB ID: 2HW7), we generated a model of MNK1 in its inactive conformation (DFD-out) and a model of MNK1 in the active conformation (DFD-in) including the phosphorylation at T209/214 (detailed in the Experimental Section). To identify the most probable binding mode of **EB1** to MNK1, we first identified the possible binding sites by molecular docking and then determined the stability of the ligand−protein complexes by MD simulation.

In the active form of MNK1, the **EB1**-MNK1 complex was broken during the simulation, indicating that the interaction found in the docking study was not stable over time. The ligand did not remain in the ATP binding site and the **EB1** molecule left the initial position before completion of the simulation (<40 ns). In contrast, the interactions formed in the inactive model of MNK1 were stable over time (Figure 5A). Based on these results, we conclude that the most probable binding of **EB1** occurs to an allosteric binding site adjacent to the ATP binding pocket, presenting the inactive conformation of MNK1. Based on the classification of protein kinase inhibitors,[29,52] the compound would therefore represent a Type II MNK1 inhibitor.

Finally, we performed interaction studies based on the molecular model of **EB1** in complex with MNK1. Hydrogen bonds are formed between the 3-aminopyrazole moiety and MNK1 (Glu125 and Gln128), confirming the importance of the presence of the unsubstituted 3-aminopyrazole ring (Figure 5B). Besides these hydrogen bonds, a hydrophobic interaction with Leu55 of MNK1 may in addition stabilize this interaction. Moreover, the phenyl ring found in position C4 of the pyrazolo[3,4-*b*]pyridine scaffold occupies the hydrophobic cleft in the most internal part of the ATP binding pocket increasing the affinity and stability of the complex (Figure 5C).

In addition to these stabilizing interactions, **EB1** interacts with the phenylalanine residue (Phe192) of the DFD motif. This $\pi-\pi$ interaction is formed between the Phe192 and the phenyl on position C6 of the pyridine ring and is maintained during all the simulation (Figure 5D). As previously reported, the change from the inactive to the active form of MNK1 results in a slightly different shape of the ATP binding pocket but is mainly characterized by the flip of the Phe192 residue from the ATP binding site. While the change in the shape of the ATP binding pocket should not interfere with the formation of the other interactions described above, the $\pi-\pi$ interaction between Phe192 and the phenyl on position C6 of the pyridine ring will not be possible in the active conformation.

Therefore, our modeling data demonstrate a stable interaction with MNK1 in its inactive conformation (Figure 5E) and the interaction with Phe192 indicates that **EB1** might prevent the flip-out of the DFD motif and thereby prevent ATP binding and kinase activity. Remarkably, the DFD motif is a unique feature of MNKs that induces the proteins to adopt an unusual stable inactive conformation, which is not common for other kinases.

https://doi.org/10.1021/acs.jmedchem.1c01941
J. Med. Chem. 2022, 65, 6070−6087

EB1 Blocks MNK Activity without Paradoxical Activation of MNK Functions. Having identified a biologically active inhibitor of MNK1 with a novel model of action, we finally compared the activity and selectivity of **EB1** to the classical ATP-competitive inhibitors CGP57380 (**2**) and eFT508 (**3**) in cell-based assays. Based on eIF4E phosphorylation as a readout for MNK activity, **EB1** appears to be more potent than CGP5738 but less active than the eFT508 (Figure 6A). The activating phosphorylation of MNK1 at T209/214 by the upstream kinases p38 and ERK was not affected by **EB1**, supporting that reduction in eIF4E phosphorylation in cells is a direct consequence of targeting the kinase activity of MNKs. These results are in striking difference from both Type I inhibitors, which strongly induced phosphorylation of MNKs at T209/214, rendering the kinase in an activated state. This paradoxical feature of certain Type I kinase inhibitors—induction of the activated state of the kinase while blocking the kinase activity—has been described before.[35,36] In the case of CGP57380 (**2**), increased phosphorylation at T209/214 has been reported previously.[29,53] Having **EB1** as an inhibitor with a novel mode of action, we aimed next at deciphering the consequences of inhibiting the kinase activity of MNK1 by different modes of action.

As detailed above, MNKs possess a specific regulatory mechanism, in which the kinase activity is autoinhibited by the conversion of the activation segment into an autoinhibitory module.[24] The release of this autoinhibition requires phosphorylation of MNKs by p38 or ERK.[23,24]

To test the efficacy of **EB1** after stimulation of MNK kinase activity, MDA-MB-231 cells were pretreated for 3 h with **EB1** or eFT508 (**3**), exposed to UV irradiation, and recovered for 40 min in the presence of the inhibitors. In line with previous reports, UV irradiation strongly increases the activating MNK1 phosphorylation at T209/214 and consequently increases the phosphorylation of eIF4E (Figure 6B). Also, under these conditions, **EB1** strongly inhibited eIF4E phosphorylation and did not affect the phosphorylation of MNK1 at T209/214. Moreover, activation of p38 (p-p38) and phosphorylation of its downstream effector HSP27 were not affected. Although p-ERK and its substrate p-p90-RSK appeared slightly elevated in **EB1**-treated cells, this effect would rather counteract inhibition of MNKs and similar effects were observed with the other MNK inhibitors tested. These results therefore indicate that **EB1** acts directly on MNK kinases without perturbing activating upstream signaling. Moreover, pretreatment of cells with **EB1** appears to maintain MNK1 in the inactive conformation even when the signaling of the activating upstream kinases is enhanced, which supports our molecular dynamics studies.

In comparison to **EB1**, striking differences in the activation state of MNK1 could be also after UV irradiation, when cells were treated with eFT508 (**3**). While **EB1** did not alter the phosphorylation of MNK1 at T209/214, MNK1 was hyper-phosphorylated in eFT508-treated cells (Figure 6A). Similar to **EB1**, upstream p38 signaling was not affected by eFT508. The increase in ERK activity after eFT508 treatment may account for the activation of MNK1. However, as the same occurs with **EB1**, this possibility appears to be rather unlikely but cannot be ruled out rigorously at this point.

In summary, ATP-competitive MNK inhibitors, while being effective in inhibiting the kinase activity, strongly alter the turnover of the phosphorylation event at T209/214 and induce hyper-phosphorylation of the activation loop, which might be caused by promoting the adaption of the kinase into the active conformation. According to our data, **EB1** inhibits the kinase activity by preventing the adaption into the active conformation and might thereby also prevent MNKs from being hyper-phosphorylated.

Importantly, phosphorylation of MNK1 has been shown to not only activate its kinase activity but also to enhance its binding to the eukaryotic initiation factor 4G (eIF4G), a scaffold protein of the translation initiation complex.[54] We therefore hypothesized that the hyper-phosphorylation of MNK1 upon eFT508 treatment should result in increased binding to eIF4G. To test this, we immuno-precipitated endogenous eIF4G from HEK-293 cells and tested for interaction with MNK1 by western blotting (Figure 6C). The treatment scheme combining UV and MNK inhibitors was the same as described above. Also, in HEK-293 cells, treatment with **EB1** did not alter the phosphorylation of state of MNK1 at T209/T214 compared to the respective control (Figure 6C, input). Moreover, stronger phosphorylation of MNK1 could be detected after treatment with eFT508 and the combination with UV irradiation resulted in hyper-phosphorylation of MNK1 at T209/T214. Under all tested conditions, MNK1 binding to eIF4G strictly correlated with the phosphorylation of MNK1 at T209/214, and consequently, the strongest interaction of eIF4G with MNK1 could be detected with hyper-phosphorylated MNK1 after UV irradiation of eFT508-treated cells. On the contrary, **EB1** treatment, while inhibiting eIF4E phosphorylation to a similar extent to eFT508, did not alter the interaction between MNK1 and eIF4G following UV irradiation. This furthermore supports our hypothesis that **EB1** acts different from the classical ATP-competitive inhibitors, by preventing the kinase to adopt its active conformation, which is not only a prerequisite for the induction of the kinase activity but also for the interaction with eIF4G.

Finally, we aimed at addressing if the different mode of action of MNK1 inhibition causes distinct cellular phenotypes. Previous reports indicate that MNK1 degradation by VNLG-152R but not inhibition of the kinase activity by eFT508 caused a reduced number of viable MDA-MB-231 cells *in vitro*.[51] In line with this, knock-down of MNK1 has been reported to affect cell growth in different cancer cell line models *in vitro*.[49,50] We therefore compared cell growth inhibition between the eFT508 and **EB1**. In line with the above results, **EB1** treatment caused a dose-dependent growth defect in MDA-MB-231 with a maximal reduction to 60% at 20 μM (Figure 6E). Importantly, this concentration does not affect cell growth of normal IMR90 cells (Figures 4C and S4C). In line with previous reports, treatment with eFT508 up to 200 nM was not able to inhibit the growth of MDA-MB-231 cells (Figures 4C and S4C).[51] However, complete inhibition of eIF4E phosphorylation can be already observed at low nanomolar concentrations of eFT508 (Figure 6A).

In summary, our molecular docking studies revealed that **EB1** binds with the highest affinity to the inactive form of MNK1. The accompanied inhibition of the MNK1 kinase activity therefore suggests that **EB1** acts as Type II kinase inhibitor and prevents the adoption of the active state of the MNK1 kinase domain. Acquisition of the active state is a prerequisite for not only MNK1 kinase activity but also interaction with eIF4G. While the kinase activity can be efficiently blocked with different types of kinase inhibitors, only ATP-competitive inhibitors enhance the interaction of MNK1

https://doi.org/10.1021/acs.jmedchem.1c01941
J. Med. Chem. 2022, 65, 6070−6087

with eIF4G (Figure 6D). The differences in the mode of action of MNK1 inhibitors might ultimately result in different cellular phenotypes as exemplified by the inhibition of cellular growth of tumor cells, which is not affected by ATP-competitive inhibitors but by **EB1**.

CONCLUSIONS

We describe here the identification and validation of the novel MNK inhibitor **EB1** and compare its mode of action to the currently available ATP-competitive inhibitors.

Starting from the scaffolds of previously reported MNK inhibitors, we systematically designed and synthesized three families of compounds and tested a total of 68 compounds in *in vitro* kinase assays. Within the family of pyrazolo[3,4-*b*]pyridin-3-amines, we identified the first hit compound **EB1**. Subsequently, several derivatives were designed, synthesized, and tested in *in vitro* and in cell-culture-based assays. The activity profile of this set of compounds confirmed the activity of the core structure as MNK inhibitors and allowed us to perform a first SAR, which revealed that the unsubstituted 3-aminopyrazole ring and aryl groups on positions C4 and C6 of the pyridine ring are important for the activity of the compound.

A detailed characterization of **EB1** revealed a higher affinity for MNK1 compared to MNK2, a fast and sustained mode of action of **EB1** in cell culture and a selective inhibition of tumor cells growth, while normal cells were not affected. Based on the previously described genetic models, this selectivity profile should be expected when blocking the function of MNKs and therefore support specificity of **EB1**. Studies combining molecular docking and molecular dynamics (MD) revealed that **EB1** binds to the inactive form of MNK1 (DFD-out), which is typically seen for Type-II kinase inhibitors. Based on these data, we set out to compare **EB1** as the first validated Type-II MNK inhibitor to the classical ATP-competitive inhibitors. This comparison finally revealed that while both types of MNK inhibitors efficiently block the kinase activity, ATP-competitive inhibitors appear to induce a pseudo-activated state of the kinase, defined by T209/214 hyper-phosphorylation through the upstream priming kinases. Yet, phosphorylation of MNKs at T209/214 has been reported to be required for eIF4G binding,[54] and consequently, an enhanced binding of MNK1 to eIF4G can be observed only in the presence of Type-I inhibitors. While the structural roles of MNK1 beyond its catalytic activity have not yet been studied in detail, it is reasonable to believe that this might have implications on the functionality of the eIF4F complex. Supporting this, many other protein kinases, including the MNK upstream kinases ERK and p38, have been reported to carry out additional functions such as scaffolding.[55] Moreover, genetic ablation of MNK1, in which both structural and catalytic activities are impaired, has been reported to block tumor cell growth[49,50] and only the novel MNK inhibitor **EB1** is able to phenocopy this.

Kinases are attractive, "druggable" targets, and after the clinical approval of the first kinase inhibitor Imatinib in 2001, 73 kinase inhibitors have received US FDA by 2021.[56,57] Remarkably though, while Imatinib is a Type II kinase inhibitor, previous analyses have revealed that the vast majority of inhibitors (33 of 42) are classified as Type I inhibitors and only six (including Imatinib) are Type II.[58] Despite the remarkable clinical success of several of those drugs, resistance to kinase inhibitors through paradoxical activation of the target pathway currently limits the success of some of those inhibitors. Paradoxical activation of the target pathway was first described by Okuzumi et al.[59] as unintended activation following inhibitor binding to the kinase. In recent years, inhibitors of many other protein kinases, including the mutated form of BRAF (BRAFV600E),[60,61] PKB,[62] PKC,[63] PKD,[64] AMPK,[65] c-Src,[66] and ERK5,[67] have been described. Remarkably, in most of these cases, ATP-competitive binding of the inhibitors induce conformational changes, which activate noncatalytic functions of these kinases.[37,68]

Our work has revealed that in the case of ATP-competitive MNK inhibitors, binding to the catalytic site promotes MNK priming by the upstream kinases and recruitment to eIF4G, while inactivation of MNKs by **EB1** induces neither kinase priming nor recruitment to eIF4G, which might thereby prevent unintended activation or priming of MNK functions.

In recent years, the eIF4E phosphorylating kinases MNK1/2 have emerged as eligible targets for drug discovery in oncology. Interference with the eIF4E/MNK axis, through either genetic models or the use of knock-down techniques, resulted in promising antitumor effects and the lack of adverse effects in dual MNK knock-out animals opened up the possibility to develop nontoxic anticancer drugs. Based on the wide knowledge on ATP-competitive inhibitors from other protein kinases and the available crystal structures of MNKs, highly efficient and selective inhibitors have been developed in recent years and some of those, like eFT508 (**3**), BAY1143269, and ETC-206, have entered clinical trial phases. The results of the Phase I studies confirmed their safety, as predicted for targeting MNKs.

We have identified and validated now a novel MNK inhibitor **EB1**. Based on homology modeling and molecular simulations, we predict **EB1** to be a Type II kinase inhibitor because it interacts with the DFD motif, a unique feature of MNKs and selectively binds to the inactive form of MNK1. This binding mode of **EB1** might ultimately resemble closer the well-studied knock-out models of MNKs than Type I inhibitors because structural functions of the activated kinase might be blocked in addition. Dissecting this aspect in preclinical models will be key to elucidate in the future, if the mainly genetic-based proposal of targeting MNKs as a promising new strategy in oncology can be better achieved with Type I or Type II inhibitors of MNK1/2.

EXPERIMENTAL SECTION

Chemistry. *General Information.* All solvents and chemicals were of reagent grade. Unless otherwise mentioned, all solvents and chemicals were purchased from commercial vendors (Sigma-Aldrich, ABCR, Fluorochem, and Acros Organics) and used without purification. ^{1}H- and ^{13}C NMR spectra were recorded on a Varian 400-MR spectrometer (^{1}H NMR at 400 MHz and ^{13}C NMR at 100.6 MHz). Chemical shifts were reported in parts per million (δ) and are referenced to the residual signal of the solvent DMSO-d_6 (2.5 ppm in ^{1}H NMR and 39.5 ppm in ^{13}C NMR). Coupling constants are reported in hertz (Hz). Standard and peak multiplicities are designed as follows: s, singlet; d, doublet; dd, doublet of doublets; dt, doublet of triplets t, triplet; q, quadruplet; qn, quintuplet; br, broad signal. HRMS data were obtained using a micrOTOF (Bunker) high-resolution spectrometer (EI, ESI or APCI mode). Elemental microanalyses were performed on a EuroVector Instruments Euro EA 3000 elemental analyzer. The melting points were determined with an SMP3 melting point apparatus (Stuart Scientific) and are uncorrected. Automatic flash chromatography was performed in an Isco Combiflash medium-pressure liquid chromatograph with RediSep silica gel columns (35−70 μm) or basic alumina columns

https://doi.org/10.1021/acs.jmedchem.1c01941
J. Med. Chem. 2022, 65, 6070−6087

using a suitable mixture of solvents as an eluent. Microwave irradiation experiments were carried out in an Initiator (Biotage) microwave apparatus, operating at a frequency of 2.45 GHz with continuous irradiation power from 0 to 400 W. Reactions were carried out in 2.5, 5, and 20 mL glass tubes sealed with aluminum/Teflon crimp tops, which can be exposed up to 250 °C and 20 bar internal pressure. Temperature was measured with an IR sensor on the outer surface of the process vial. After the irradiation period, the reaction vessel was cooled rapidly to 50 °C by air jet cooling.

Purity Statement. Purity (≥95%) of the compounds for this study was confirmed by elemental analysis (within ±0.4% of the calculated value). Additionally, lead compounds were tested by HPLC (see the Supporting Information).

*6-Chloro-5-(2,6-dichlorophenyl)-2-phenyl-2H-pyrazolo[3,4-b]-pyridin-3-amine (**5a**).* 3-Amino-5-(2,6-dichlorophenyl)-2-phenyl-2,4,5,7-tetrahydro-6*H*-pyrazolo [3,4-*b*]pyridine-6-one (**S15e**) (50 mg, 0.1 mmol) was suspended in 3 mL of $POCl_3$. The mixture was refluxed for 3 h at 120 °C. The $POCl_3$ was removed under reduced pressure, and the crude was resuspended in water and neutralized with $NaHCO_3$. The solid was filtered and purified by column chromatography (alumina column, Cy:AcOEt gradient 0 to 60% in 30 min) to give 13 mg (10%) of 6-chloro-5-(2,6-dichlorophenyl)-2-phenyl-2*H*-pyrazolo[3,4-*b*]pyridin-3-amine (**5a**) as a yellowish solid.

Mp: >250 °C. ^{1}H NMR (400 MHz, DMSO-d_6): δ 8.16 (s, 1H), 7.73−7.69 (m, 2H), 7.67−7.59 (m, 4H), 7.55−7.48 (m, 2H), 6.95 (s, 2H). ^{13}C NMR (100 MHz, DMSO-d_6): δ 155.8, 151.3, 142.9, 138.5, 136.5, 135.8, 135.6, 131.5, 129.9, 128.7, 128.7, 125.1, 120.0, 101.1.

*5,6-Dichloro-2,4-diphenyl-2H-pyrazolo[3,4-b]pyridin-3-amine (**5b**).* 3-Amino-4-phenyl-2-phenyl-2,4,5,7-tetrahydro-6*H*-pyrazolo[3,4-*b*]pyridine-6-one (**S15h**) (100 mg, 0.33 mmol) and 341 mg (1.64 mmol) of PCl_5 were dissolved in 2.5 mL of $POCl_3$, and the mixture was refluxed for 18 h. The mixture was poured into ice, and the precipitate was filtered and washed with water. The solid was then resuspended in water, and the suspension was neutralized with $NaHCO_3$. The solid was filtered and dried *in vacuo* over P_2O_5 to yield 5,6-dichloro-2,4-diphenyl-2*H*-pyrazolo[3,4-*b*]pyridin-3-amine (**5b**) in 72% yield.

Mp: 130−133 °C. ^{1}H NMR (400 MHz, DMSO-d_6): δ 7.67−7.56 (m, 7H), 7.55−7.48 (m, 3H), 5.02 (s, 2H). ^{13}C NMR (100 MHz, DMSO-d_6): δ 153.4, 149.8, 146.0, 140.8, 137.6, 133.3, 129.7, 129.6, 129.1, 128.7, 128.3, 124.9, 115.2, 100.1. HRMS (ESI) *m*/*z*: calculated for $C_{18}H_{13}Cl_2N_4$ $[M + 1]^+$: 355.0512; found $[M + 1]^+$: 355.0513.

*General Method for the Synthesis of 2-Methoxynicotinonitriles (**9**).* NaOMe (101 mg, 1.87 mmol) was dissolved in 5 mL of MeOH in a microwave vial. Arylketone (**7**) (1.7 mmol) and arylaldehyde (**8**) (1.7 mmol) were added and the mixture was stirred for 5 min at room temperature. Then, 1.7 mmol of malononitrile were added and the reaction was heated under microwave irradiation for 5 min at 140 °C. The solvent was removed under reduced pressure. The solid obtained was resuspended in MeOH and filtered to afford the corresponding 2-methoxynicotinonitrile (**9**).

*2-Methoxy-4,6-bis(4-methoxyphenyl)nicotinonitrile (**9e**).* Starting from 1-(4-methoxyphenyl)ethan-1-one and 4-methoxybenzaldehyde. 20% yield, yellowish solid. Mp: 184−186 °C. ^{1}H NMR (400 MHz, DMSO-d_6): δ 8.28−8.19 (m, 2H), 7.76−7.68 (m, 3H), 7.17−7.11 (m, 2H), 7.10−7.04 (m, 2H), 4.12 (s, 3H), 3.85 (s, 6H). ^{13}C NMR (100 MHz, DMSO-d_6): δ 164.4, 161.4, 160.7, 156.9, 155.7, 130.2, 129.1, 128.0, 115.8, 114.3, 112.5, 109.5, 90.7, 55.4, 55.4, 54.3. Elemental analysis: calculated for $C_{21}H_{18}N_2O_3$: C: 72.82%, H: 5.24%, N: 8.09%; found: C: 72.94%, H: 5.40%, N: 8.11%.

*2-Methoxy-6-(4-methoxyphenyl)-4-(p-tolyl)nicotinonitrile (**9f**).* Starting from 1-(4-methoxyphenyl)ethan-1-one and 4-methylbenzaldehyde. 33% yield, yellowish solid. Mp: 189−191 °C. ^{1}H NMR (400 MHz, DMSO-d_6): δ 8.27−8.22 (m, 2H), 7.71 (s, 1H), 7.67−7.62 (m, 2H), 7.42−7.37 (m, 2H), 7.10−7.06 (m, 2H), 4.13 (s, 3H), 3.84 (s, 3H), 2.41 (s, 3H). ^{13}C NMR (100 MHz, DMSO-d_6): δ 164.3, 161.4, 157.0, 156.1, 139.9, 133.1, 129.4, 129.2, 129.1, 128.5, 115.7, 114.3, 112.6, 91.0, 55.4, 54.4, 20.9. HRMS (APCI) *m*/*z*: calculated for $C_{21}H_{19}N_2O_2$ $[M + 1]^+$: 331.1441; found $[M + 1]^+$: 331.1440.

*2-Methoxy-6-(3-methoxyphenyl)-4-phenylnicotinonitrile (**9g**).* Starting from 1-(3-methoxyphenyl)ethan-1-one and benzaldehyde. 20% yield, white solid. Mp: 153−155 °C. ^{1}H NMR (400 MHz, DMSO-d_6): δ 7.88−7.86 (m, 1H), 7.85 (s, 1H), 7.80−7.78 (m, 1H), 7.77−7.73 (m, 2H), 7.61−7.57 (m, 3H), 7.48−7.44 (m, 1H), 7.13−7.08 (m, 1H), 4.15 (s, 3H), 3.85 (s, 3H). ^{13}C NMR (100 MHz, DMSO-d_6): δ 164.2, 159.7, 157.1, 156.4, 138.1, 135.8, 130.0, 130.0, 128.8, 128.7, 119.9, 116.4, 115.3, 114.0, 112.7, 92.4, 55.3, 54.5. HRMS (APCI) *m*/*z*: calculated for $C_{20}H_{17}N_2O_2$ $[M + 1]^+$: 317.1285; found $[M + 1]^+$: 317.1282.

*2-Methoxy-6-(2-methoxyphenyl)-4-(4-methoxyphenyl)-nicotinonitrile (**9h**).* Starting from 1-(2-methoxyphenyl)ethan-1-one and 4-methoxybenzaldehyde. 65% yield, yellowish solid. Mp: 131−133 °C. ^{1}H NMR (400 MHz, DMSO-d_6): δ 8.01−7.94 (m, 1H), 7.74 (s, 1H), 7.70−7.65 (m, 2H), 7.54−7.46 (m, 1H), 7.24−7.19 (m, 1H), 7.17−7.11 (m, 3H), 4.09 (s, 3H), 3.87 (s, 3H), 3.85 (s, 3H). ^{13}C NMR (100 MHz, DMSO-d_6): δ 164.1, 160.7, 157.4, 155.9, 154.8, 131.6, 130.9, 130.0, 128.1, 126.1, 120.8, 117.9, 115.6, 114.4, 112.3, 91.2, 55.8, 55.4, 54.4. HRMS (APCI) *m*/*z*: calculated for $C_{21}H_{19}N_2O_3$ $[M + 1]^+$: 347.1390; found $[M + 1]^+$: 347.1387.

*2-Methoxy-6-(2-methoxyphenyl)-4-(p-tolyl)nicotinonitrile (**9i**).* Starting from 1-(2-methoxyphenyl)ethan-1-one and 4-methylbenzaldehyde. 88% yield, yellowish solid. Mp: 157−159 °C. ^{1}H NMR (400 MHz, DMSO-d_6): δ 8.01−7.97 (m, 1H), 7.74 (s, 1H), 7.62−7.56 (m, 2H), 7.53−7.46 (m, 1H), 7.41−7.37 (m, 2H), 7.23−7.19 (m, 1H), 7.16−7.10 (m, 1H), 4.10 (s, 3H), 3.87 (s, 3H), 2.40 (s, 3H). ^{13}C NMR (100 MHz, DMSO-d_6): δ 164.0, 157.4, 156.0, 155.2, 139.9, 133.1, 131.7, 130.9, 129.5, 128.3, 126.0, 120.8, 118.1, 115.5, 112.3, 91.5, 55.8, 54.5, 20.9.

*4-(4-Fluorophenyl)-2-methoxy-6-(3-methoxyphenyl)-nicotinonitrile (**9j**).* Starting from 1-(3-methoxyphenyl)ethan-1-one and 4-fluorobenzaldehyde. 25% yield, white solid. Mp: 157−159 °C. ^{1}H NMR (400 MHz, DMSO-d_6): δ 7.91−7.74 (m, 5H), 7.52−7.40 (m, 3H), 7.18−7.07 (m, 1H), 4.15 (s, 3H), 3.85 (s, 3H). ^{13}C NMR (100 MHz, DMSO-d_6): δ 164.1, 163.2 (d, J = 248.0 Hz), 159.7, 157.1, 155.3, 138.1, 131.2 (d, J = 8.8 Hz), 130.0, 119.9, 116.3, 115.8 (d, J = 21.8 Hz), 115.3, 114.0, 112.7, 92.5, 55.3, 54.5. HRMS (APCI) *m*/*z*: calculated for $C_{20}H_{16}FN_2O_2$ $[M + 1]^+$: 335.1190; found $[M + 1]^+$: 335.1192.

*2-Methoxy-4-(4-methoxyphenyl)-6-phenylnicotinonitrile (**9k**).* Starting from acetophenone and 4-methoxybenzaldehyde. 33% yield, yellowish solid. Mp: 181−183 °C. ^{1}H NMR (400 MHz, DMSO-d_6): δ 8.30−8.24 (m, 2H), 7.80 (s, 1H), 7.78−7.72 (m, 2H), 7.58−7.51 (m, 3H), 7.18−7.11 (m, 2H), 4.15 (s, 3H), 3.86 (s, 3H). ^{13}C NMR (100 MHz, DMSO-d_6): δ 164.4, 160.8, 157.1, 155.9, 136.8, 130.6, 130.2, 128.9, 127.9, 127.4, 115.7, 114.3, 113.5, 91.8, 55.4, 54.5. HRMS (APCI) *m*/*z*: calculated for $C_{20}H_{17}N_2O_2$ $[M + 1]^+$: 317.1285; found $[M + 1]^+$: 317.1281.

*2-Methoxy-6-(3-methoxyphenyl)-4-(4-methoxyphenyl)-nicotinonitrile (**9l**).* Starting from 1-(3-methoxyphenyl)ethan-1-one and 4-methoxybenzaldehyde. 20% yield, yellowish solid. Mp: 138−140 °C. ^{1}H NMR (400 MHz, DMSO-d_6): δ 7.87−7.83 (m, 1H), 7.81 (s, 1H), 7.80−7.78 (m, 1H), 7.77−7.73 (m, 2H), 7.48−7.44 (m, 1H), 7.17−7.13 (m, 2H), 7.13−7.09 (m, 1H), 4.14 (s, 3H), 3.85 (m, 6H). ^{13}C NMR (100 MHz, DMSO-d_6): δ 164.3, 160.8, 159.7, 156.8, 155.9, 138.2, 130.3, 130.0, 127.8, 119.8, 116.2, 115.6, 114.3, 113.7, 112.7, 91.9, 55.4, 55.3, 54.4. HRMS (APCI) *m*/*z*: calculated for $C_{21}H_{19}N_2O_3$ $[M + 1]^+$: 347.1390; found $[M + 1]^+$: 347.1393.

*4-(4-Fluorophenyl)-2-methoxy-6-phenylnicotinonitrile (**9o**).* Starting from acetophenone and 4-fluorobenzaldehyde. 62% yield, yellowish solid. Mp: 165−169 °C. ^{1}H NMR (400 MHz, DMSO-d_6): δ 8.31−8.25 (m, 2H), 7.87−7.81 (m, 3H), 7.56−7.53 (m, 2H), 7.49−7.42 (m, 2H), 4.16 (s, 3H). ^{13}C NMR (100 MHz, DMSO-d_6): δ 164.3, 163.2 (d, J = 248.0 Hz), 157.3, 155.3, 136.6, 132.2 (d, J = 3.1 Hz), 131.1 (d, J = 8.8 Hz), 130.7, 128.9, 127.5, 115.9 (d, J = 21.9 Hz), 115.3, 113.8, 92.3, 54.6. HRMS (APCI) *m*/*z*: calculated for $C_{19}H_{14}FN_2O$ $[M + 1]^+$: 305.1085; found $[M + 1]^+$: 305.1081.

*General Method for the Synthesis of 2-Bromonicotinonitriles (**10**).* The corresponding 2-methoxy-nicotinonitrile (**9**) (0.6 mmol) was dissolved in 4 mL of 1,4-dioxane together with $POBr_3$ (1.34

https://doi.org/10.1021/acs.jmedchem.1c01941
J. Med. Chem. 2022, 65, 6070−6087

mmol), pyridinium HBr (0.015 mmol), and H_3PO_4 (0.026 mmol). The mixture was heated at 60 °C for 18 h under argon atmosphere and then quenched with cold water. Then, the mixture was neutralized with NaOH (6 M) and the precipitate was filtered and washed with cold water. The solid was dried *in vacuo* over P_2O_5 to yield the corresponding 2-bromonicotinonitrile (**10**).

*2-Bromo-4,6-diphenylnicotinonitrile (**10a**).* Starting from 2-methoxy-4,6-diphenylnicotinonitrile. 84% yield, white solid. Mp: 123−125 °C. ^{1}H NMR (400 MHz, DMSO-d_6): δ 8.26 (s, 1H), 8.24 (m, 2H), 7.80 (m, 2H), 7.62 (m, 3H), 7.57 (m, 3H). ^{13}C NMR (100 MHz, DMSO-d_6): δ 159.3, 156.2, 144.4, 135.5, 135.3, 131.3, 130.5, 129.1, 128.9, 127.7, 119.7, 116.5, 109.7. Elemental analysis: calculated for $C_{18}H_{11}BrN_2$: C: 64.50%, H: 3.31%, N: 8.36%; found: C: 64.83%, H: 3.58%, N: 8.31%.

*2-Bromo-nicotinonitrile (**10c**).* Starting from 2-methoxy-nicotinonitrile. 50% yield, white crystals mp: 170−172 °C. ^{1}H NMR (400 MHz, DMSO-d_6) 8.68 (dd, J = 4.9, 2.0 Hz, 1H), 8.42 (dd, J = 7.8, 2.0 Hz, 1H), 7.69 (dd, J = 7.7, 4.9 Hz, 1H). ^{13}C NMR (100 MHz, DMSO-d_6) 153.8, 143.9, 142.8, 123.5, 116.2, 113.1. Elemental analysis: calculated for $C_6H_3N_2Br$: C: 39.38%, H: 1.65%, N: 15.31%; found: C: 39.21%, H: 1.71%, N: 15.53%.

*2-Bromo-4,6-bis(4-methoxyphenyl)nicotinonitrile (**10e**).* Starting from 2-methoxy-4,6-bis(4-methoxyphenyl)nicotinonitrile (**9e**). 92% yield, white solid. Mp: 221−223 °C. ^{1}H NMR (400 MHz, DMSO-d_6): δ 8.24−8.19 (m, 2H), 8.13 (s, 1H), 7.78−7.72 (m, 2H), 7.17−7.13 (m, 2H), 7.12−7.07 (m, 2H), 3.86 (s, 3H), 3.85 (s, 3H). ^{13}C NMR (100 MHz, DMSO-d_6): δ 161.9, 161.0, 158.8, 155.6, 142.8, 130.5, 129.5, 127.9, 127.4, 120.2, 118.4, 116.9, 114.5, 114.3, 55.5, 55.5. HRMS (APCI) m/z: calculated for $C_{20}H_{16}BrN_2O_2$ $[M + 1]^+$: 395.0390; found $[M + 1]^+$: 395.0387.

*2-Bromo-6-(4-methoxyphenyl)-4-(p-tolyl)nicotinonitrile (**10f**).* Starting from 2-methoxy-6-(4-methoxyphenyl)-4-(*p*-tolyl)-nicotinonitrile (**9f**). 83% yield, orange solid. Mp: 207−209 °C. ^{1}H NMR (400 MHz, DMSO-d_6): δ 8.24−8.17 (m, 2H), 8.13 (s, 1H), 7.70−7.65 (m, 2H), 7.43−7.39 (m, 2H), 7.13−7.07 (m, 2H), 3.85 (s, 3H), 2.42 (s, 3H). ^{13}C NMR (100 MHz, DMSO-d_6): δ 161.9, 159.0, 155.9, 144.3, 140.3, 132.5, 129.5, 129.4, 128.7, 127.8, 118.5, 116.7, 114.5, 108.3, 55.5, 20.9. Elemental analysis: calculated for $C_{20}H_{15}BrN_2O$: C: 63.34%, H: 3.99%, N: 7.39%; found: C: 63.74%, H: 3.99%, N: 7.39%.

*2-Bromo-6-(3-methoxyphenyl)-4-phenylnicotinonitrile (**10g**).* Starting from 2-methoxy-6-(3-methoxyphenyl)-4-phenylnicotinonitrile (**9g**). 68% yield, brownish solid. Mp: 184−186 °C. ^{1}H NMR (400 MHz, DMSO-d_6): δ 8.29 (s, 1H), 7.85−7.82 (m, 1H), 7.80−7.77 (m, 2H), 7.76−7.74 (m, 1H), 7.64−7.59 (m, 3H), 7.50−7.45 (m, 1H), 7.17−7.12 (m, 1H), 3.86 (s, 3H). ^{13}C NMR (100 MHz, DMSO-d_6): δ 159.8, 159.0, 156.2, 144.2, 136.9, 135.3, 130.4, 130.2, 128.9, 128.8, 120.1, 120.0, 117.2, 116.5, 112.6, 109.8, 55.4. HRMS (APCI) m/z: calculated for $C_{19}H_{14}BrN_2O$ $[M + 1]^+$: 365.0284; found $[M + 1]^+$: 365.0284.

*2-Bromo-6-(2-methoxyphenyl)-4-(4-methoxyphenyl) Nicotinonitrile (**10h**).* Starting from 2-methoxy-6-(2-methoxyphenyl)-4-(4-methoxyphenyl)nicotinonitrile (**9h**). 75% yield, white solid. Mp: 197−198 °C. ^{1}H NMR (400 MHz, DMSO-d_6): δ 8.10 (s, 1H), 7.87−7.83 (m, 1H), 7.73−7.69 (m, 2H), 7.55−7.52 (m, 1H), 7.25−7.21 (m, 1H), 7.19−7.13 (m, 3H), 3.87 (s, 3H), 3.86 (s, 3H). ^{13}C NMR (100 MHz, DMSO-d_6): δ 161.0, 158.0, 157.4, 154.6, 143.9, 132.4, 130.9, 130.3, 127.4, 124.9, 123.7, 120.9, 116.7, 114.5, 112.4, 108.6, 55.9, 55.4.

*2-Bromo-6-(2-methoxyphenyl)-4-(p-tolyl)nicotinonitrile (**10i**).* Starting from 2-methoxy-6-(2-methoxyphenyl)-4-(*p*-tolyl)-nicotinonitrile (**9i**). 65% yield, brownish solid. Mp: 198−200 °C. ^{1}H NMR (400 MHz, DMSO-d_6): δ 8.11 (s, 1H), 7.88−7.83 (m, 1H), 7.65−7.59 (m, 2H), 7.57−7.51 (m, 1H), 7.43−7.39 (m, 2H), 7.26−7.21 (m, 1H), 7.18−7.12 (m, 1H), 3.87 (s, 3H), 2.41 (s, 3H). ^{13}C NMR (100 MHz, DMSO-d_6): δ 158.2, 157.5, 155.0, 143.8, 140.4, 132.5, 132.4, 131.00, 129.6, 128.6, 124.8, 123.8, 120.9, 116.6, 112.4, 108.9, 55.9, 20.9. Elemental analysis: calculated for $C_{20}H_{15}BrN_2O$: C: 63.34%, H: 3.99%, N: 7.39%; found: C: 63.26%, H: 4.03%, N: 7.12%.

*2-Bromo-4-(4-fluorophenyl)-6-(3-methoxyphenyl)nicotinonitrile (**10j**).* Starting from 4-(4-fluorophenyl)-2-methoxy-6-(3-methoxyphenyl)nicotinonitrile (**9j**). 67% yield, brownish solid. Mp: 191−195 °C. ^{1}H NMR (400 MHz, DMSO-d_6): δ 8.29 (s, 1H), 7.90−7.84 (m, 2H), 7.84−7.81 (m, 1H), 7.77−7.73 (m, 1H), 7.51−7.43 (m, 3H), 7.17−7.12 (m, 1H), 3.86 (s, 3H). ^{13}C NMR (100 MHz, DMSO-d_6): δ 163.4 (d, J = 248.3 Hz), 159.8, 159.1, 155.5, 144.2, 136.9, 131.7 (d, J = 3.1 Hz), 131.5 (d, J = 8.8 Hz), 130.3, 120.1, 120.1, 117.2, 116.5, 115.9 (d, J = 22.0 Hz), 112.7, 109.9, 55.5. Elemental analysis: calculated for $C_{19}H_{12}BrFN_2O$: C: 59.55%, H: 3.16%, N: 7.31%; found: C: 59.92%, H: 3.12%, N: 6.94%.

*2-Bromo-4-(4-methoxyphenyl)-6-phenylnicotinonitrile (**10k**).* Starting from 2-methoxy-4-(4-methoxyphenyl)-6-phenylnicotinonitrile (**9k**). 82% yield, gray solid. Mp: 214−216 °C. ^{1}H NMR (400 MHz, DMSO-d_6): δ 8.24−8.18 (m, 3H), 7.80−7.73 (m, 2H), 7.57−7.53 (m, 3H), 7.18−7.12 (m, 2H), 3.85 (s, 3H). ^{13}C NMR (100 MHz, DMSO-d_6): δ 161.1, 159.1, 155.8, 144.5, 135.5, 131.2, 130.6, 129.1, 127.6, 127.3, 119.5, 116.8, 114.3, 109.2, 55.5. HRMS (APCI) m/z: calculated for $C_{19}H_{14}BrN_2O$ $[M + 1]^+$: 365.0284; found $[M + 1]^+$: 365.0282.

*2-Bromo-6-(3-methoxyphenyl)-4-(4-methoxyphenyl)-nicotinonitrile (**10l**).* Starting from 2-methoxy-6-(3-methoxyphenyl)-4-(4-methoxyphenyl)nicotinonitrile (**9l**). 90% yield, gray solid. Mp: 219−221 °C. ^{1}H NMR (400 MHz, DMSO-d_6): δ 8.23 (s, 1H), 7.83−7.76 (m, 3H), 7.75−7.72 (m, 1H), 7.50−7.46 (m, 1H), 7.19−7.10 (m, 3H), 3.86 (s, 3H), 3.86 (s, 3H). ^{13}C NMR (100 MHz, DMSO-d_6): δ 161.1, 159.8, 158.9, 155.9, 144.4, 137.0, 130.6, 130.2, 127.3, 120.1, 119.7, 117.1, 116.8, 114.3, 112.6, 109.3, 55.5, 55.4. Elemental analysis: calculated for $C_{20}H_{15}BrN_2O_2$: C: 60.78%, H: 3.83%, N: 7.09%; found: C: 60.47%, H: 4.04%, N: 7.08%.

*2-Bromo-4-(4-fluorophenyl)-6-phenylnicotinonitrile (**10o**).* Starting from 4-(4-fluorophenyl)-2-methoxy-6-phenylnicotinonitrile (**9o**). 85% yield, brownish solid. Mp: 184−187 °C. ^{1}H NMR (400 MHz, DMSO-d_6): δ 8.26 (s, 1H), 8.25−8.21 (m, 2H), 7.91−7.83 (m, 2H), 7.60−7.54 (m, 3H), 7.50−7.44 (m, 2H). ^{13}C NMR (100 MHz, DMSO-d_6): δ 163.4 (d, J = 248.6 Hz), 159.3, 155.1, 144.3, 135.4, 131.7 (d, J = 3.0 Hz), 131.5 (d, J = 8.9 Hz), 131.3, 129.1, 127.7, 119.8, 116.5, 115.9 (d, J = 22.0 Hz), 109.8. HRMS (APCI) m/z: calculated for $C_{18}H_{11}BrFN_2$ $[M + 1]^+$: 353.0084; found $[M + 1]^+$: 353.0082.

*General Method for the Synthesis of Pyrazolo[3,4-b]pyridine-3-amines (**6**).* The corresponding 2-bromonicotinonitrile (**10**) (0.18 mmol) and hydrazine (0.36 mmol) were dissolved in 3 mL of methanol and sealed in a 5 mL microwave vial. The mixture was heated under microwave irradiation for 2 h at 140 °C and cooled rapidly. The solvent was removed under reduced pressure, and the crude was resuspended in methanol. The solid was filtered, washed with methanol, and dried *in vacuo* over P_2O_5 to yield the corresponding pyrazolo[3,4-*b*]pyridine-3-amine (**6**).

*1-Methyl-4,6-diphenyl-1H-pyrazolo[3,4-b]pyridin-3-amine (**6a**).* Starting from 2-bromo-4,6-diphenylnicotinonitrile (**10a**) and methylhydrazine. 57% yield, yellow solid. Mp: 176−177 °C. ^{1}H NMR (400 MHz, DMSO-d_6): δ 8.27−8.21 (m, 2H), 7.72−7.67 (m, 2H), 7.62−7.44 (m, 6H), 7.49 (s, 1H), 4.66 (s, 2H), 3.90 (s, 3H). ^{13}C NMR (100 MHz, DMSO-d_6): δ 155.4, 151.3, 146.2, 145.7, 138.7, 137.0, 129.4, 129.0, 128.9, 128.7, 128.7, 127.2, 112.1, 102.2, 32.7. Elemental analysis: calculated for $C_{20}H_{18}N_4O$: C: 72.71%, H: 5.49%, N: 16.96%; found: C: 72.72%, H: 5.43%, N: 16.66%.

*4,6-Diphenyl-1H-pyrazolo[3,4-b]pyridin-3-amine (**6b**, **EB1**).* Starting from 2-bromo-4,6-diphenylnicotinonitrile (**10a**) and hydrazine monohydrate. Purification by column chromatography (silica column, Cy:AcOEt gradient 0 to 20% in 10 min, 20% isocratic for 5 min and 20−100% in 15 min). 71% yield, yellow solid. Mp: 219−220 °C. ^{1}H NMR (400 MHz, DMSO-d_6): δ 12.37 (s, 1H), 8.21−8.15 (m, 2H), 7.73−7.67 (m, 2H), 7.63−7.47 (m, 6H), 7.48 (s, 1H), 4.56 (s, 2H). ^{13}C NMR (100 MHz, DMSO-d_6): δ 155.5, 153.3, 147.2, 145.3, 138.9, 137.2, 129.2, 128.9, 128.8, 128.8, 128.7, 127.2, 112.4, 102.0. Elemental analysis: calculated for $C_{18}H_{14}N_4$: C: 75.50%, H: 4.90%, N: 19.60%; found: C: 75.43%, H: 4.90%, N: 19.56%.

https://doi.org/10.1021/acs.jmedchem.1c01941
J. Med. Chem. 2022, 65, 6070−6087

*1H-Pyrazolo[3,4-b]pyridin-3-amine (**6c**).* Starting from 2-bromonicotinonitrile (**10c**) and hydrazine monohydrate. 57% yield, orange solid. Mp: 162−164 °C. ^{1}H NMR (400 MHz, DMSO-d_6): δ 11.90 (s, 1H), 8.33 (dd, J = 4.6, 1.6 Hz, 1H), 8.11 (dd, J = 7.9, 1.6 Hz, 1H), 6.94 (dd, J = 7.9, 4.5 Hz, 1H), 5.55 (s, 2H). ^{13}C NMR (100 MHz, DMSO-d_6): δ 152.3, 148.5, 148.1, 129.7, 113.8, 106.2.

*1-Methyl-1H-pyrazolo[3,4-b]pyridin-3-amine (**6d**).* Starting from 2-bromonicotinonitrile (**10c**) and methylhydrazine. 43% yield, yellow solid. Mp: 115−116 °C. ^{1}H NMR (400 MHz, DMSO-d_6): δ 8.36 (dd, J = 4.5, 1.6 Hz, 1H), 8.10 (dd, J = 7.9, 1.6 Hz, 1H), 6.95 (dd, J = 7.9, 4.6 Hz, 1H), 5.66 (s, 2H), 3.75 (s, 3H). ^{13}C NMR (100 MHz, DMSO-d_6): δ 150.5, 148.6, 147.2, 129.9, 113.6, 106.5, 32.5. Elemental analysis: calculated for $C_7H_8N_4$: C: 56.74%, H: 5.40%, N: 37.80%; found: C: 56.93%, H: 5.30%, N: 37.40%.

*4,6-Bis(4-methoxyphenyl)-1H-pyrazolo[3,4-b]pyridin-3-amine (**6e**).* Starting from 2-bromo-4,6-bis(4-methoxyphenyl)nicotinonitrile (**10e**) and hydrazine monohydrate. 65% yield, yellow solid. Mp: 228−230 °C. ^{1}H NMR (400 MHz, DMSO-d_6): δ 12.23 (s, 1H), 8.19−8.02 (m, 2H), 7.71−7.56 (m, 2H), 7.38 (s, 1H), 7.16−7.11 (m, 2H), 7.07−7.02 (m, 2H), 4.56 (s, 2H), 3.85 (s, 3H), 3.82 (s, 3H). ^{13}C NMR (100 MHz, DMSO-d_6): δ 160.3, 159.8, 155.2, 153.4, 147.2, 145.0, 131.4, 130.1, 129.5, 128.5, 114.3, 114.1, 111.6, 101.6, 55.3, 55.2. HRMS (APCI) m/z: calculated for $C_{20}H_{19}N_4O_2$ $[M + 1]^+$: 347.1503; found $[M + 1]^+$: 347.1499.

*6-(4-Methoxyphenyl)-4-(p-tolyl)-1H-pyrazolo[3,4-b]pyridin-3-amine (**6f**).* Starting from 2-bromo-6-(4-methoxyphenyl)-4-(*p*-tolyl)-nicotinonitrile (**10f**) and hydrazine monohydrate. 47% yield, yellow solid. Mp: 203−207 °C. ^{1}H NMR (400 MHz, DMSO-d_6): δ 12.25 (s, 1H), 8.17−8.10 (m, 2H), 7.61−7.53 (m, 2H), 7.42−7.37 (m, 3H), 7.08−7.02 (m, 2H), 4.53 (s, 2H), 3.82 (s, 3H), 2.42 (s, 3H). ^{13}C NMR (100 MHz, DMSO-d_6): δ 160.3, 155.2, 153.3, 147.1, 145.2, 138.4, 134.4, 131.4, 129.4, 128.6, 128.5, 114.1, 111.6, 101.5, 55.2, 20.9. HRMS (APCI) m/z: calculated for $C_{20}H_{19}N_4O$ $[M + 1]^+$: 331.1553; found $[M + 1]^+$: 331.1554.

*6-(3-Methoxyphenyl)-4-phenyl-1H-pyrazolo[3,4-b]pyridin-3-amine (**6g**, **EB2**).* Starting from 2-bromo-6-(3-methoxyphenyl)-4-phenylnicotinonitrile (**10g**) and hydrazine monohydrate. Purification by column chromatography (silica column, Cy:AcOEt gradient 0−40% in 20 min and then isocratic at 40% for 30 min). 60% yield, yellow solid. Mp: >250 °C. ^{1}H NMR (400 MHz, DMSO-d_6): δ 12.38 (s, 1H), 7.78−7.73 (m, 1H), 7.73−7.67 (m, 3H), 7.63−7.53 (m, 3H), 7.49 (s, 1H), 7.42−7.40 (m, 1H), 7.07−7.00 (m, 1H), 4.56 (s, 2H), 3.85 (s, 3H). ^{13}C NMR (100 MHz, DMSO-d_6): δ 159.6, 155.3, 153.2, 147.1, 145.3, 140.4, 137.1, 129.8, 128.9, 128.8, 128.8, 119.6, 115.2, 112.5, 112.1, 102.1, 55.2. Elemental analysis: calculated for $C_{20}H_{18}N_4O$: C: 72.71%, H: 5.49%, N: 16.96%; found: C: 72.71%, H: 5.46%, N: 16.63%.

*6-(2-Methoxyphenyl)-4-(4-methoxyphenyl)-1H-pyrazolo[3,4-b]-pyridin-3-amine (**6h**).* Starting from 2-bromo-6-(2-methoxyphenyl)-4-(4-methoxyphenyl)nicotinonitrile (**10h**) and hydrazine monohydrate. Purification by column chromatography (silica column, Cy:AcOEt gradient 0−70% for 25 min, then isocratic at 70% for 45 min). 55% yield, yellowish solid. Mp: 236−238 °C. ^{1}H NMR (400 MHz, DMSO-d_6): δ 12.27 (s, 1H), 7.74−7.68 (m, 1H), 7.62−7.56 (m, 2H), 7.45−7.40 (m, 1H), 7.31 (s, 1H), 7.19−7.12 (m, 3H), 7.11−7.05 (m, 1H), 4.58 (s, 2H), 3.84 (s, 3H), 3.82 (s, 3H). ^{13}C NMR (100 MHz, DMSO-d_6): δ 159.8, 156.9, 154.9, 153.2, 147.1, 143.6, 130.9, 130.1, 130.0, 129.5, 128.9, 120.6, 116.5, 114.3, 112.0, 101.4, 55.6, 55.3. Elemental analysis: calculated for $C_{20}H_{18}N_4O_2$: C: 69.35%, H: 5.24%, N: 16.17%; found: C: 69.60%, H: 5.64%, N: 16.57%.

*6-(2-Methoxyphenyl)-4-(p-tolyl)-1H-pyrazolo[3,4-b]pyridin-3-amine (**6i**).* Starting from 2-bromo-6-(2-methoxyphenyl)-4-(*p*-tolyl)-nicotinonitrile (**10i**) and hydrazine monohydrate. Purification by column chromatography (silica column, Cy:AcOEt gradient 0−70% in 40 min). 60% yield, yellowish solid. Mp: 219−220 °C. ^{1}H NMR (400 MHz, DMSO-d_6): δ 12.29 (s, 1H), 7.74−7.70 (m, 1H), 7.55−7.52 (m, 2H), 7.46−7.41 (m, 1H), 7.41−7.36 (m, 2H), 7.32 (s, 1H), 7.18−7.13 (m, 1H), 7.11−7.05 (m, 1H), 4.55 (s, 2H), 3.81 (s, 3H), 2.41 (s, 3H). ^{13}C NMR (100 MHz, DMSO-d_6): δ 156.9, 154.9, 153.2, 147.1, 143.8, 138.3, 134.4, 130.9, 130.2, 129.5, 128.8, 128.6, 120.6, 116.5, 112.0, 101.3, 55.6, 20.9. HRMS (APCI) m/z: calculated for $C_{20}H_{19}N_4O$ $[M + 1]^+$: 331.1553; found $[M + 1]^+$: 331.1552.

*4-(4-Fluorophenyl)-6-(3-methoxyphenyl)-1H-pyrazolo[3,4-b]pyridin-3-amine (**6j**).* Starting from 2-bromo-4-(4-fluorophenyl)-6-(3-methoxyphenyl)nicotinonitrile (**10j**) and hydrazine monohydrate. 50% yield, yellow solid. Mp: 194−195 °C. ^{1}H NMR (400 MHz, DMSO-d_6): δ 12.39 (s, 1H), 7.80−7.69 (m, 4H), 7.49 (s, 1H), 7.45−7.36 (m, 3H), 7.05−7.01 (m, 1H), 4.60 (s, 2H), 3.85 (s, 3H). ^{13}C NMR (100 MHz, DMSO-d_6): δ 162.6 (d, J = 245.8 Hz), 159.6, 155.2, 153.2, 147.2, 144.3, 140.4, 133.4 (d, J = 3.1 Hz), 131.1 (d, J = 8.4 Hz), 129.8, 119.6, 115.6 (d, J = 21.6 Hz), 115.2, 112.6, 112.2, 102.1, 55.2. HRMS (APCI) m/z: calculated for $C_{19}H_{16}FN_4O$ $[M + 1]^+$: 335.1303; found $[M + 1]^+$: 335.1298.

*4-(4-Methoxyphenyl)-6-phenyl-1H-pyrazolo[3,4-b]pyridin-3-amine (**6k**).* Starting from 2-bromo-4-(4-methoxyphenyl)-6-phenylnicotinonitrile (**10k**) and hydrazine monohydrate. 64% yield, brownish solid. Mp: 196−198 °C. ^{1}H NMR (400 MHz, DMSO-d_6): δ 12.32 (s, 1H), 8.19−8.12 (m, 2H), 7.69−7.64 (m, 2H), 7.55−7.42 (m, 4H), 7.18−7.13 (m, 2H), 4.60 (s, 2H), 3.85 (s, 3H). ^{13}C NMR (100 MHz, DMSO-d_6): δ 159.9, 155.4, 153.4, 147.2, 145.2, 139.0, 130.2, 129.3, 129.2, 128.7, 127.1, 114.3, 112.2, 102.0, 55.3. HRMS (APCI) m/z: calculated for $C_{19}H_{17}N_4O$ $[M + 1]^+$: 317.1397; found $[M + 1]^+$: 317.1393.

*6-(3-Methoxyphenyl)-4-(4-methoxyphenyl)-1H-pyrazolo[3,4-b]-pyridin-3-amine (**6l**).* Starting from 2-bromo-6-(3-methoxyphenyl)-4-(4-methoxyphenyl)-nicotinonitrile (**10l**) and hydrazine monohydrate. 48% yield, yellowish solid. Mp: 191−193 °C. ^{1}H NMR (400 MHz, DMSO-d_6): δ 12.32 (s, 1H), 7.76−7.72 (m, 1H), 7.71−7.69 (m, 1H), 7.68−7.63 (m, 2H), 7.45−7.38 (m, 2H), 7.17−7.12 (m, 2H), 7.05−7.01 (m, 1H), 4.60 (s, 2H,), 3.85 (s, 3H), 3.85 (s, 3H). ^{13}C NMR (100 MHz, DMSO-d_6): δ 159.9, 159.6, 155.2, 153.3, 147.2, 145.1, 140.5, 130.2, 129.8, 129.3, 119.6, 115.1, 114.3, 112.3, 112.1, 102.2, 55.3, 55.2. Elemental analysis: calculated for $C_{20}H_{18}N_4O_2$: C: 69.35%, H: 5.24%, N: 16.17%; found: C: 69.40%, H: 5.44%, N: 15.80%.

*4,6-Bis(4-methoxyphenyl)-1-methyl-1H-pyrazolo[3,4-b] pyridin-3-amine (**6m**).* Starting from 2-bromo-4,6-bis(4-methoxyphenyl)-nicotinonitrile (**10e**) and methylhydrazine. 81% yield, yellowish solid. Mp: 192−195 °C. ^{1}H NMR (400 MHz, DMSO-d_6): δ 8.23−8.16 (m, 2H), 7.68−7.60 (m, 2H), 7.39 (s, 1H), 7.17−7.12 (m, 2H), 7.10−7.03 (m, 2H), 4.65 (s, 2H), 3.87 (s, 3H), 3.85 (s, 3H), 3.83 (s, 3H). ^{13}C NMR (100 MHz, DMSO-d_6): δ 160.4, 159.9, 155.1, 151.4, 146.3, 145.3, 131.2, 130.1, 129.3, 128.6, 114.3, 114.1, 111.3, 101.8, 55.3, 55.3, 32.7. Elemental analysis: calculated for $C_{21}H_{20}N_4O_2$: C: 69.98%, H: 5.59%, N: 15.55%; found: C: 69.59%, H: 5.67%, N: 15.83%.

*4-(4-Methoxyphenyl)-1-methyl-6-phenyl-1H-pyrazolo[3,4-b] pyridin-3-amine (**6n**).* Starting from 2-bromo-4-(4-methoxyphenyl)-6-phenylnicotinonitrile (**10k**) and methylhydrazine. 75% yield, yellowish solid. Mp: 192−194 °C. ^{1}H NMR (400 MHz, DMSO-d_6): δ 8.25−8.20 (m, 2H), 7.68−7.63 (m, 2H), 7.55−7.46 (m, 3H), 7.45 (s, 1H), 7.16−7.12 (m, 2H), 4.69 (s, 2H), 3.89 (s, 3H), 3.85 (s, 3H). ^{13}C NMR (100 MHz, DMSO-d_6): δ 160.0, 155.3, 151.4, 146.3, 145.5, 138.8, 130.2, 129.3, 129.1, 128.7, 127.2, 114.3, 111.9, 102.3, 55.3, 32.7. Elemental analysis: calculated for $C_{20}H_{18}N_4O$: C: 72.71%, H: 5.49%, N: 16.96%; found: C: 72.72%, H: 5.43%, N: 16.66%.

*4-(4-Fluorophenyl)-6-phenyl-1H-pyrazolo[3,4-b]pyridin-3-amine (**6o**, **EB3**).* Starting from 2-bromo-4-(4-fluorophenyl)-6-phenylnicotinonitrile (**10o**) and hydrazine monohydrate. 48% yield, yellowish solid. Mp: 194−199 °C. ^{1}H NMR (400 MHz, DMSO-d_6): δ 12.38 (s, 1H), 8.20−8.16 (m, 2H), 7.79−7.73 (m, 2H), 7.54−7.45 (m, 4H), 7.44−7.38 (m, 2H), 4.61 (s, 2H). ^{13}C NMR (100 MHz, DMSO-d_6): δ 162.6 (d, J = 245.7 Hz), 155.5, 153.3, 147.2, 144.3, 138.9, 133.5 (d, J = 3.2 Hz), 131.1 (d, J = 8.4 Hz), 129.2, 128.7, 127.2, 115.7 (d, J = 21.6 Hz), 112.5, 102.0. HRMS (APCI) m/z: calculated for $C_{18}H_{14}FN_4$ $[M + 1]^+$: 305.1197; found $[M + 1]^+$: 305.1197.

Computational Methods. *Preparation of MNK1 Structures.* The inactive unphosphorylated model was created using the available crystal structure of MNK1 (PDB ID: 2HW6[24]). The tertiary structure of the missing fragments was predicted *de novo* by applying the loop modeler module available in MOE2016.08 [Molecular Operating

https://doi.org/10.1021/acs.jmedchem.1c01941
J. Med. Chem. 2022, 65, 6070−6087

Environment (MOE), 2016.08. Chemical Computing Group ULC, 1010 Sherbooke St. West, Suite #910, Montreal, QC, Canada, H3A 2R7 (2016)]. The best loop candidate was energy-minimized by performing a short molecular dynamics (MD) simulation, using AMBER software [Case, D. A. et al. AMBER 14. University of California, San Francisco (2014)].

The tridimensional structure of the active phosphorylated MNK1 model was obtained by homology modeling using the active MNK2 model as a template, which was obtained from the MNK2 D228G crystal structure (PDB ID: 2HW7), manually reverted the mutation G228D and prepared with the same protocol used for MNK1. The sequence of MNK1 and the MNK2 model were aligned in MOE2016.08, and the tridimensional structure was created based on the tertiary structure of the MNK2 model obtaining the active MNK1 structure. Finally, Thr209 and Thr214 residues were manually phosphorylated.

The two models were then submitted to an MD simulation. The system was subjected to a first minimization including a 5000-step minimization of TIP3P water molecules followed by a 20 000-step energy minimization of the entire system. Then, heated to 300 K in 200 ps using the Langevin thermostat restraining the backbone atoms except the loop atoms using an 8 kcal·mol^{-1}·Å^{-2} force constant. Pressure equilibration (1 atm) was performed for 1000 ps maintaining the restraints previously described. The SHAKE algorithm[69] was used throughout to restrain the bonds involving hydrogens and the particle mesh Ewald[70] method for long-range electrostatic, while the short-range interactions had an 8 Å cutoff radius. The production stage was extended to at least 70 ns defining a 2 fs time-step (until root-mean-square deviation (RMSD) was stable). Amber ff13 force field was used for the parameters of standard amino acids. The parameters described by Homeyer et al. were used for phosphorylated amino acids.[71]

Finally, an accelerated MD (aMD) simulation was performed to explore the accessible conformational space. The parameters used in each of the aMD simulations were calculated from the corresponding MD simulation and are the following for the inactive and active model, respectively: average total potential energy threshold (E(tot)): −205630.72 and −147028; inverse strength boost factor for the total potential energy (α(tot)): 14664.6 and 10465; average dihedral energy threshold (E(dih)): 383.8 and 343.2; inverse strength boost factor for the dihedral energy (α(dih)): 209.3 and 206.

The simulations were extended until the RMSD values were stable: 90000 steps for the inactive model and 120 000 steps for the active model. All MD simulations in this study were performed in a 4.20 GHz × 8 Intel Core i7-7700K processor with 16 GB RAM and a GeForce GTX 1050 Ti GPU. Cluster analysis was performed with CPPTRAJ.[72] For each simulation, the most populated and stable cluster was selected as the representative structure of each state of the protein.

Complex Preparation and MD Simulation. For each model, the most plausible active site was identified by blind docking, using MOE2016.08 on a 2.6 GHz Intel Core i7-6700HQ with 8 GB RAM. Docking poses were generated using the triangle matcher placement method (1000 poses) with the induced fit protocol and scored using London ΔG scoring function and GBVI/WSA ΔG for rescoring (100 poses). The most populated cluster was defined as the active site. For each model, a conformation of the ligand found in the identified active site was selected to study the interaction with the protein.

An MD simulation was performed for each ligand−protein complex using the same conditions previously described. The production stage was extended to at least 50 ns defining a 2 fs time-step (until RMSD was stable).

Characterization of the Interactions. The study of the hydrogen-bond pattern was performed using CPPTRAJ.[72] Hydrogen bonds were determined using simple geometric criteria such as the donor to acceptor heavy atom distance.

Ligand−protein interactions were visualized with MOE2016.08 (MOE2016.08. Chemical Computing Group ULC, 1010 Sherbooke St. West, Suite #910, Montreal, QC, Canada, H3A 2R7 (2016)).

MNK1 and MNK2 Enzymatic In Vitro Assay. *Measurement of the Residual Activity.* Determination of the effect of the compounds on the kinase activity of MNKs (and other kinases) *in vitro* was performed with a radiometric protein kinase assay (^{33}PanQinase Activity Assay) at Reaction Biology (www.reactionbiology.com). Protein kinases were purchased from Life Technologies (Invitrogen Corporation). The compounds were provided as solids and were dissolved to 1 × 10^{-3} M stock solutions in 100% DMSO (100 × stock). The 10 × stock solution was prepared by dissolving 10 μL of the 100 × stock in 90 μL of water resulting in a 1 × 10^{-4} M/10% DMSO solution.

The final working concentration was 1 × 10^{-5} M, resulting in a final concentration of 1% DMSO. Active compounds were tested in replicates as indicated.

Protein Kinase Assay. A radiometric protein kinase assay (^{33}PanQinase Activity Assay) was used for measuring the kinase activity of the two protein kinases MNK1 and MNK2. All kinase assays were performed in 96-well FlashPlatesTM from PerkinElmer (Boston, MA) in a 50 μL reaction volume. The reaction cocktail was pipetted in four steps in the following order: (1) 20 μL of assay buffer, (2) 5 μL of ATP solution (in H_2O), (3) 5 μL of test compound (in 10% DMSO), and (4) 20 μL of enzyme−substrate mixture.

The assay for all protein kinases contained 70 mM HEPES−NaOH pH 7.5, 3 mM $MgCl_2$, 3 mM $MnCl_2$, 3 μM Na-orthovanadate, 1.2 mM DTT, 50 μg/mL PEG_{20000}, ATP (variable amounts, corresponding to the apparent ATP-K_m of the respective kinase, 1 μM for MNK1 and 0.3 μM for MNK2), [γ-^{33}P]-ATP (approx. 1.2 × 10^6 cpm per well), protein kinase (variable amounts depending on the stock), and substrate (S6 peptide, 2 μg/50 μL).

The reaction cocktails were incubated at 30 °C for 60 min. The reaction was stopped with 50 μL of 2% (v/v) H_3PO_4, and the plates were aspirated and washed two times with 200 μL of 0.9% (w/v) NaCl. The incorporation of ^{33}Pi was determined with a microplate scintillation counter (Microbeta, Wallac). All assays were performed with a Beckman Coulter/SAGIAN Core System.

Evaluation of Raw Data. The residual activity (in %) for each well of a particular plate was calculated using the following formula

$$\text{Res. activity (\%)} = 100 \times [(\text{cpm of compound} - \text{low control}) / (\text{high control} - \text{low control})]$$

where cpm is the counts per minute measured for the mix containing the compound, "low control" reflects unspecific binding of radioactivity to the plate in the absence of a protein kinase but in the presence of the substrate, and "high control" is full activity in the absence of any inhibitor. The difference between high and low controls was taken as 100% activity.

Quality Controls. As a parameter for assay quality, the Z'-factor 10838414[73] for the low and high controls of each assay plate (n = 8) was used. Reaction Biology's criterion for repetition of an assay plate is a Z'-factor below 0.4.[74]

Determination of the IC_{50}. The IC_{50} profile of the compounds was determined using the previously described radiometric protein kinase assay (^{33}PanQinase Activity Assay). IC_{50} values were measured by testing 10 concentrations of the compounds in the range of 5 × 10^{-5} to 1.5 × 10^{-9} M.

Cell-Culture-Based Experiments. *Cell Culture and Reagents.* Breast cancer cell lines were purchased from the American Type Culture Collection (ATCC). MDA-MB-231, MDA-MB-468, MCF7, A375M, IMR90, and HEK-293 cells were grown in DMEM (Dulbecco's modified Eagle's medium: 4.5 g/L D-glucose; 580 mg/L L-Glutamine (Gibco)) supplemented with 10% heat-inactivated fetal bovine serum (FBS) (Life Technologies), 100 U/mL penicillin, and 100 μg/mL streptomycin (Life Technologies).

MV4-11 cells were grown in IMDM medium (Iscove's modified Dulbecco's medium, Gibco) supplemented with 10% FBS, 1% L-glutamine, 100 U/mL penicillin, and 100 μg/mL streptomycin.

Prostate cancer cell line 22Rv1 was obtained from ATCC. Cells were cultured in RPMI-1640 (Biowest) supplemented with 10% heat-inactivated FBS, 2 mM L-glutamine, 1% penicillin-streptomycin

https://doi.org/10.1021/acs.jmedchem.1c01941
J. Med. Chem. 2022, 65, 6070−6087

solution, 1% MEM non-essential amino acids, and 1% sodium pyruvate (all from Biowest). The cells were maintained at 37 °C in a 5% CO_2 humidified incubator.

Inhibitors and Cell Treatment. For inhibitor treatments, the cells were seed in at a density of 6000 cells/cm^2 in the respective plates 24 h before the treatment. Compounds were diluted to the final concentration in a medium maintaining DMSO at a concentration below 0.5%. DMSO was used as the negative control, and CGP57380 (Merck) and eFT508 (Selleckchem) were used for comparison.

UV Treatment. MDA-MB-231 or HEK293T cells were incubated with the indicated concentrations of MNK1/2 inhibitors for 24 h and then irradiated with UV (60 J/m^2) followed by 40 min incubation at 37 °C. Total cell lysates were analyzed by immunoblotting with the indicated antibodies.

Cristal Violet Growth Assay. The cells were seeded in a 24- or 96-well plate at a density of 6000 cells/cm^2, and after 24 h, treatments were carried out. After the corresponding time, the medium was removed and the cells were fixed with 4% formaldehyde solution for 30 min and washed twice with phosphate-buffered saline (PBS). The cells were stained with crystal violet solution (0.5% in water) for 15 min, washed extensively with water, and air-dried. Crystal violet was dissolved in 200 μL of 15% AcOH, and the optical density of the solution was measured at 595 nm (Epoch Microplate Spectrophotometer, BioTek).

Propidium Iodide-Hoechst-Based Analysis of Cell Death. Prior to fixation of cells for the crystal violet assay, propidium iodide (2.5 μM) and Hoechst (0.05 mg/mL) in complete culture medium was added to the cells without removal of the culture medium, incubated for 30 min, and representative pictures were taken from each well using a Nikon Eclipse TE2000-S microscope. A minimum of 100 cells were counted per experimental condition, and the percentage of PI-positive cells among the Hoechst positive cells was determined.

Sulforhodamine B (SRB) Cytotoxicity Assay. Cells were seeded at a density of 5000 cells per well in a 96-well tissue culture plate. After 24 h, the cells were treated with different concentrations of MNK1/2 inhibitors. Control cultures received the same amount of DMSO as did the treated cultures. Doxorubicin at a 1 μM concentration was used as a positive control. On day 3, cell numbers were calculated using the SRB assay. The SRB assay was performed following protocols adapted from Euglossa Orellana (2016) with minor modifications.[75] Briefly, the medium was discarded and the adherent cells were fixed *in situ* by adding to each well 100 μL of cold trichloroacetic acid 10% (w/v) and incubating for 60 min at 4 °C. The plates were then washed four times with deionized water and air-dried. Each well then received 100 μL of SRB (Merck, S1402-5G) solution (0.04% w/v in 1% acetic acid), and the plates were incubated for 1 h at room temperature. Unbound SRB was removed by washing four times with 1% acetic acid. Then, the plates were air-dried. Bound stain was solubilized with 100 μL of 10 mM unbuffered Tris base (pH 10.5), and the optical densities were read using a microtiter plate reader at 510 nm. Four replicates were used for each analysis. The percentage of growth inhibition was calculated using the equation: % Growth Inhibition = $(1 - N_t/N_c) \times 100$, where N_t and N_c represent the absorbance in treated and untreated cultures, respectively.

Flow Cytometry. The effect of **EB1** on the cell cycle of MDA-MB-231 cells was analyzed by flow cytometry measurement of propidium iodide (PI)-stained cells. In brief, 1×10^6 cells were seeded in 10 cm plates and treated with the indicated concentrations of compounds for 72 h. The cells were trypsinized, washed twice with PBS, resuspended in 0.3 mL of PBS, and fixed by the addition of 0.7 mL of ice-cold absolute EtOH under continuous agitation. The cells were fixed for 2 h on ice. For PI staining, the cells were pelleted and the supernatant was discarded and washed twice with PBS. The cells were suspended in staining solution (RNAse A (300 μg/mL, Sigma), sodium citrate (1.14 mM), and propidium iodide (15 μg/mL, Sigma)) and incubated at 4 °C overnight. DNA content was measured using a FACS Fortessa instrument integrated with FACS Diva (BD Biosciences).

Protein Extraction and Immunoblotting. Total protein extracts were generated using lysis buffer (50 mM Tris-HCl, pH 7.4, 150 mM NaCl, 1% Triton X-100, 1% sodium deoxycholate, 0.1% SDS, 1 mM EDTA) supplemented with PhosSTOP and Complete Phosphatase/Protease Inhibitor Cocktails (Roche Diagnostics GmbH, Mannheim, Germany). Protein extracts (20−25 μg per sample) were loaded onto sodium dodecyl sulfate-polyacrylamide gel electrophoresis (SDS-PAGE) gels and transferred electrophoretically to poly(vinylidene fluoride) (PVDF) membranes. The following primary antibodies were used at a dilution of 1:1000: ERK1/2 (p44/42) (ab17942, Abcam), p-ERK1/2 (p-p44/42) (Thr202/Tyr204) (9101, Cell Signaling), MNK1 (2195, Cell Signaling), p-MNK1 (Thr197/202) (2111, Cell Signaling), eIF4E (9742, Cell Signaling), p-eIF4E (p-Ser 209) (9741, Cell Signaling or NBP2-66802, Novus Biologicals), p38alpha (9218, Cell Signaling), p38beta (2339, Cell Signaling), p-p38 (4511, Cell Signaling), p-ATF2 (27934, Cell Signaling), Hsp27 (2402, Cell Signaling), p-Hsp27 (S82) (2401, Cell Signaling), and p-p90 RSK (Thr573) (9346, Cell Signaling). The primary HRP-conjugated antibody anti-β-actin (Calbiochem) was used at a dilution of 1:20 000. Anti-mouse and anti-rabbit HRP secondary antibodies were from Pierce and used at a dilution of 1:10 000. Immunodetection of proteins was performed using ECL Western Blotting Detection Reagents (GE Healthcare, Buckinghamshire, U.K.).

Immunoprecipitation. Cells were lysed with lysis buffer (50 mM Tris-HCl pH 7.5, 150 mM NaCl, 1% NP-40, 5 mM EGTA, 5 mM EDTA) including protease and phosphatase inhibitor cocktails (PhosSTOP and Complete). Immunoprecipitation of eIF4G was performed using anti-eIF4G antibodies (Santa Cruz Biotechnology) and Pierce Protein A agarose beads (Thermo Scientific) following the manufacturer's indications. Briefly, beads were incubated in 300 μL of ice-cold PBS containing 3 μL of anti-eIF4G antibodies for 4 h rotating at 4 °C. Then, the beads were washed three times in cold PBS and incubated in 500 μL of ice-cold precleared lysates containing approximately 2 mg of cell lysate overnight rotating at 4 °C. The next day beads were recovered by washing twice in ice-cold lysis buffer and resuspended in 1× loading buffer, boiled at 95 °C for 5 min, and analyzed by SDS-PAGE and immunoblotting.

■ ASSOCIATED CONTENT

Supporting Information

The Supporting Information is available free of charge at https://pubs.acs.org/doi/10.1021/acs.jmedchem.1c01941.

Molecular formula strings (CSV)

NMR spectra of the compounds mentioned in the main text, the synthesis of initial candidates from Figures S2 and S3, HPLC spectra of the lead compounds, and PDB coordinates for the EB1-MNK1 complex (PDF)

■ AUTHOR INFORMATION

Corresponding Authors

Stefan Hümmer − *Translational Molecular Pathology, Vall d'Hebron Research Institute (VHIR), Universitat Autònoma de Barcelona, 08035 Barcelona, Spain; Spanish Biomedical Research Network Centre in Oncology (CIBERONC), 28029 Madrid, Spain*; Email: stefan.hummer@vhir.org

José I. Borrell − *Grup de Química Farmacèutica, IQS School of Engineering, Universitat Ramon Llull, 08017 Barcelona, Spain*; Email: jose.borrell@iqs.url.edu

Santiago Ramón y Cajal − *Translational Molecular Pathology, Vall d'Hebron Research Institute (VHIR), Universitat Autònoma de Barcelona, 08035 Barcelona, Spain; Spanish Biomedical Research Network Centre in Oncology (CIBERONC), 28029 Madrid, Spain*; orcid.org/0000-0002-3867-1390; Email: sramon@vhebron.net

https://doi.org/10.1021/acs.jmedchem.1c01941
J. Med. Chem. 2022, 65, 6070−6087

Authors

Elisabeth Bou-Petit − *Grup de Química Farmacèutica, IQS School of Engineering, Universitat Ramon Llull, 08017 Barcelona, Spain*

Helena Alarcon − *Grup de Química Farmacèutica, IQS School of Engineering, Universitat Ramon Llull, 08017 Barcelona, Spain*

Konstantin Slobodnyuk − *Translational Molecular Pathology, Vall d'Hebron Research Institute (VHIR), Universitat Autònoma de Barcelona, 08035 Barcelona, Spain; Spanish Biomedical Research Network Centre in Oncology (CIBERONC), 28029 Madrid, Spain*

Marta Cano-Galietero − *Translational Molecular Pathology, Vall d'Hebron Research Institute (VHIR), Universitat Autònoma de Barcelona, 08035 Barcelona, Spain; Spanish Biomedical Research Network Centre in Oncology (CIBERONC), 28029 Madrid, Spain*

Pedro Fuentes − *Translational Molecular Pathology, Vall d'Hebron Research Institute (VHIR), Universitat Autònoma de Barcelona, 08035 Barcelona, Spain; Spanish Biomedical Research Network Centre in Oncology (CIBERONC), 28029 Madrid, Spain;* Present Address: Laboratory of Cancer Metabolism, ONCOBELL Program, Bellvitge Biomedical Research Institute (IDIBELL), Barcelona, Spain

Pedro J. Guijarro − *Translational Molecular Pathology, Vall d'Hebron Research Institute (VHIR), Universitat Autònoma de Barcelona, 08035 Barcelona, Spain*

María José Muñoz − *Translational Molecular Pathology, Vall d'Hebron Research Institute (VHIR), Universitat Autònoma de Barcelona, 08035 Barcelona, Spain; Spanish Biomedical Research Network Centre in Oncology (CIBERONC), 28029 Madrid, Spain*

Leticia Suarez-Cabrera − *Cell Cycle and Cancer Laboratory, Biomedical Research Group in Urology, Vall d'Hebron Research Institute (VHIR), Universitat Autònoma de Barcelona, 08035 Barcelona, Spain*

Anna Santamaria − *Cell Cycle and Cancer Laboratory, Biomedical Research Group in Urology, Vall d'Hebron Research Institute (VHIR), Universitat Autònoma de Barcelona, 08035 Barcelona, Spain*

Roger Estrada-Tejedor − *Grup de Química Farmacèutica, IQS School of Engineering, Universitat Ramon Llull, 08017 Barcelona, Spain;* orcid.org/0000-0002-2983-0492

Complete contact information is available at: https://pubs.acs.org/10.1021/acs.jmedchem.1c01941

Author Contributions

#E.B.-P. and S.H. contributed equally. The manuscript was written through contributions of all authors. All authors have given approval to the final version of the manuscript.

Funding

This work was supported by the Instituto de Salud Carlos III (PI17/02247), (PI20/01687), and CIBERONC (CB16/12/00363). S.R.y.C. acknowledges support from the Generalitat de Catalunya (2017-9015-385045). E. Bou-Petit thanks the Secretaria d'Universitats i Recerca del Departament d'Economia i Coneixement de la Generalitat de Catalunya (2017 FI_B2 00139) and the European Social Funds for her predoctoral fellowship.

Notes

The authors declare no competing financial interest.

■ ACKNOWLEDGMENTS

The authors thank Juan A. Recio and Jose M. Lizcano for critically reading the manuscript and for helpful comments and suggestions. The authors thankfully acknowledge the computer resources at Minotauro and technical support provided by Barcelona Supercomputing Center (BCV-2015-2-0001, BCV-2015-3-0009, and BCV-2016-3-0016).

■ ABBREVIATIONS (NONSTANDARD)

AMPK, AMP-activated protein kinase; eIF4F, eukaryotic translation initiation complex 4F; eIF4E, eukaryotic translation initiation factor 4E; eIF4G, eukaryotic translation initiation factor 4G; FACS, fluorescence-activated cell sorting; FBS, fetal bovine serum; MNK1/2, MAP kinase interacting kinases 1/2; PI, propidium iodide; PKD, protein kinase D

■ REFERENCES

(1) Ramón y Cajal, S.; Castellvi, J.; Hummer, S.; Peg, V.; Pelletier, J.; Sonenberg, N. Beyond molecular tumor heterogeneity: protein synthesis takes control. *Oncogene* **2018**, *37*, 2490−2501.

(2) Bhat, M.; Robichaud, N.; Hulea, L.; Sonenberg, N.; Pelletier, J.; Topisirovic, I. Targeting the translation machinery in cancer. *Nat. Rev. Drug Discovery* **2015**, *14*, 261−278.

(3) Sonenberg, N.; Hinnebusch, A. G. Regulation of translation initiation in eukaryotes: mechanisms and biological targets. *Cell* **2009**, *136*, 731−745.

(4) Proud, C. G. Mnks, eIF4E phosphorylation and cancer. *Biochim. Biophys. Acta, Gene Regul. Mech.* **2015**, *1849*, 766−773.

(5) Siddiqui, N.; Sonenberg, N. Signalling to eIF4E in cancer. *Biochem. Soc. Trans.* **2015**, *43*, 763−772.

(6) Wendel, H. G.; Silva, R. L.; Malina, A.; Mills, J. R.; Zhu, H.; Ueda, T.; Watanabe-Fukunaga, R.; Fukunaga, R.; Teruya-Feldstein, J.; Pelletier, J.; Lowe, S. W. Dissecting eIF4E action in tumorigenesis. *Genes Dev.* **2007**, *21*, 3232−3237.

(7) Zhan, Y.; Guo, J.; Yang, W.; Goncalves, C.; Rzymski, T.; Dreas, A.; Zylkiewicz, E.; Mikulski, M.; Brzozka, K.; Golas, A.; Kong, Y.; Ma, M.; Huang, F.; Huor, B.; Guo, Q.; da Silva, S. D.; Torres, J.; Cai, Y.; Topisirovic, I.; Su, J.; Bijian, K.; Alaoui-Jamali, M. A.; Huang, S.; Journe, F.; Ghanem, G. E.; Miller, W. H., Jr.; Del Rincon, S. V. MNK1/2 inhibition limits oncogenicity and metastasis of KIT-mutant melanoma. *J. Clin. Invest.* **2017**, *127*, 4179−4192.

(8) Robichaud, N.; del Rincon, S. V.; Huor, B.; Alain, T.; Petruccelli, L. A.; Hearnden, J.; Goncalves, C.; Grotegut, S.; Spruck, C. H.; Furic, L.; Larsson, O.; Muller, W. J.; Miller, W. H.; Sonenberg, N. Phosphorylation of eIF4E promotes EMT and metastasis via translational control of SNAIL and MMP-3. *Oncogene* **2015**, *34*, 2032−2042.

(9) Beggs, J. E.; Tian, S.; Jones, G. G.; Xie, J.; Iadevaia, V.; Jenei, V.; Thomas, G.; Proud, C. G. The MAP kinase-interacting kinases regulate cell migration, vimentin expression and eIF4E/CYFIP1 binding. *Biochem. J.* **2015**, *467*, 63−76.

(10) Piccirillo, C. A.; Bjur, E.; Topisirovic, I.; Sonenberg, N.; Larsson, O. Translational control of immune responses: from transcripts to translatomes. *Nat. Immunol.* **2014**, *15*, 503−511.

(11) Joshi, S.; Platanias, L. C. Mnk Kinases in Cytokine Signaling and Regulation of Cytokine Responses. *Biomol. Concepts* **2012**, *3*, 127−139.

(12) Xu, Y.; Poggio, M.; Jin, H. Y.; Shi, Z.; Forester, C. M.; Wang, Y.; Stumpf, C. R.; Xue, L.; Devericks, E.; So, L.; Nguyen, H. G.; Griselin, A.; Gordan, J. D.; Umetsu, S. E.; Reich, S. H.; Worland, S. T.; Asthana, S.; Barna, M.; Webster, K. R.; Cunningham, J. T.; Ruggero, D. Translation control of the immune checkpoint in cancer and its therapeutic targeting. *Nat. Med.* **2019**, *25*, 301−311.

(13) Pinto-Díez, C.; Ferreras-Martin, R.; Carrion-Marchante, R.; Gonzalez, V. M.; Martin, M. E. Deeping in the Role of the MAP-Kinases Interacting Kinases (MNKs) in Cancer. *Int. J. Mol. Sci.* **2020**, *21*, 2967.

(14) Huang, F.; Goncalves, C.; Bartish, M.; Remy-Sarrazin, J.; Issa, M. E.; Cordeiro, B.; Guo, Q.; Emond, A.; Attias, M.; Yang, W.; Plourde, D.; Su, J.; Gimeno, M. G.; Zhan, Y.; Galan, A.; Rzymski, T.; Mazan, M.; Masiejczyk, M.; Faber, J.; Khoury, E.; Benoit, A.; Gagnon, N.; Dankort, D.; Journe, F.; Ghanem, G. E.; Krawczyk, C. M.; Saragovi, H. U.; Piccirillo, C. A.; Sonenberg, N.; Topisirovic, I.; Rudd, C. E.; Miller, W. H., Jr.; Del Rincon, S. V. Inhibiting the MNK1/2-eIF4E axis impairs melanoma phenotype switching and potentiates antitumor immune responses. *J. Clin. Invest.* **2021**, *131*, No. e140752.
(15) Waskiewicz, A. J.; Flynn, A.; Proud, C. G.; Cooper, J. A. Mitogen-activated protein kinases activate the serine/threonine kinases Mnk1 and Mnk2. *EMBO J.* **1997**, *16*, 1909−1920.
(16) Martínez-Sáez, E.; Peg, V.; Ortega-Aznar, A.; Martinez-Ricarte, F.; Camacho, J.; Hernandez-Losa, J.; Ferreres Pinas, J. C.; Ramon, Y. C. S. peIF4E as an independent prognostic factor and a potential therapeutic target in diffuse infiltrating astrocytomas. *Cancer Med.* **2016**, *5*, 2501−2512.
(17) Adesso, L.; Calabretta, S.; Barbagallo, F.; Capurso, G.; Pilozzi, E.; Geremia, R.; Delle Fave, G.; Sette, C. Gemcitabine triggers a pro-survival response in pancreatic cancer cells through activation of the MNK2/eIF4E pathway. *Oncogene* **2013**, *32*, 2848−2857.
(18) Grzmil, M.; Seebacher, J.; Hess, D.; Behe, M.; Schibli, R.; Moncayo, G.; Frank, S.; Hemmings, B. A. Inhibition of MNK pathways enhances cancer cell response to chemotherapy with temozolomide and targeted radionuclide therapy. *Cell. Signalling* **2016**, *28*, 1412−1421.
(19) Geter, P. A.; Ernlund, A. W.; Bakogianni, S.; Alard, A.; Arju, R.; Giashuddin, S.; Gadi, A.; Bromberg, J.; Schneider, R. J. Hyperactive mTOR and MNK1 phosphorylation of eIF4E confer tamoxifen resistance and estrogen independence through selective mRNA translation reprogramming. *Genes Dev.* **2017**, *31*, 2235−2249.
(20) D'Abronzo, L. S.; Bose, S.; Crapuchettes, M. E.; Beggs, R. E.; Vinall, R. L.; Tepper, C. G.; Siddiqui, S.; Mudryj, M.; Melgoza, F. U.; Durbin-Johnson, B. P.; deVere White, R. W.; Ghosh, P. M. The androgen receptor is a negative regulator of eIF4E phosphorylation at S209: implications for the use of mTOR inhibitors in advanced prostate cancer. *Oncogene* **2017**, *36*, 6359−6373.
(21) Slentz-Kesler, K.; Moore, J. T.; Lombard, M.; Zhang, J.; Hollingsworth, R.; Weiner, M. P. Identification of the human Mnk2 gene (MKNK2) through protein interaction with estrogen receptor beta. *Genomics* **2000**, *69*, 63−71.
(22) Fukunaga, R.; Hunter, T. MNK1, a new MAP kinase-activated protein kinase, isolated by a novel expression screening method for identifying protein kinase substrates. *EMBO J.* **1997**, *16*, 1921−1933.
(23) Jauch, R.; Jakel, S.; Netter, C.; Schreiter, K.; Aicher, B.; Jackle, H.; Wahl, M. C. Crystal structures of the Mnk2 kinase domain reveal an inhibitory conformation and a zinc binding site. *Structure* **2005**, *13*, 1559−1568.
(24) Jauch, R.; Cho, M. K.; Jakel, S.; Netter, C.; Schreiter, K.; Aicher, B.; Zweckstetter, M.; Jackle, H.; Wahl, M. C. Mitogen-activated protein kinases interacting kinases are autoinhibited by a reprogrammed activation segment. *EMBO J.* **2006**, *25*, 4020−4032.
(25) Roux, P. P.; Blenis, J. ERK and p38 MAPK-activated protein kinases: a family of protein kinases with diverse biological functions. *Microbiol. Mol. Biol. Rev.* **2004**, *68*, 320−344.
(26) Altman, J. K.; Szilard, A.; Konicek, B. W.; Iversen, P. W.; Kroczynska, B.; Glaser, H.; Sassano, A.; Vakana, E.; Graff, J. R.; Platanias, L. C. Inhibition of Mnk kinase activity by cercosporamide and suppressive effects on acute myeloid leukemia precursors. *Blood* **2013**, *121*, 3675−3681.
(27) Konicek, B. W.; Stephens, J. R.; McNulty, A. M.; Robichaud, N.; Peery, R. B.; Dumstorf, C. A.; Dowless, M. S.; Iversen, P. W.; Parsons, S.; Ellis, K. E.; McCann, D. J.; Pelletier, J.; Furic, L.; Yingling, J. M.; Stancato, L. F.; Sonenberg, N.; Graff, J. R. Therapeutic inhibition of MAP kinase interacting kinase blocks eukaryotic initiation factor 4E phosphorylation and suppresses outgrowth of experimental lung metastases. *Cancer Res.* **2011**, *71*, 1849−1857.
(28) Bain, J.; Plater, L.; Elliott, M.; Shpiro, N.; Hastie, C. J.; McLauchlan, H.; Klevernic, I.; Arthur, J. S.; Alessi, D. R.; Cohen, P. The selectivity of protein kinase inhibitors: a further update. *Biochem. J.* **2007**, *408*, 297−315.
(29) Dreas, A.; Mikulski, M.; Milik, M.; Fabritius, C. H.; Brzozka, K.; Rzymski, T. Mitogen-activated Protein Kinase (MAPK) Interacting Kinases 1 and 2 (MNK1 and MNK2) as Targets for Cancer Therapy: Recent Progress in the Development of MNK Inhibitors. *Curr. Med. Chem.* **2017**, *24*, 3025−3053.
(30) Reich, S. H.; Sprengeler, P. A.; Chiang, G. G.; Appleman, J. R.; Chen, J.; Clarine, J.; Eam, B.; Ernst, J. T.; Han, Q.; Goel, V. K.; Han, E. Z. R.; Huang, V.; Hung, I. N. J.; Jemison, A.; Jessen, K. A.; Molter, J.; Murphy, D.; Neal, M.; Parker, G. S.; Shaghafi, M.; Sperry, S.; Staunton, J.; Stumpf, C. R.; Thompson, P. A.; Tran, C.; Webber, S. E.; Wegerski, C. J.; Zheng, H.; Webster, K. R. Structure-based Design of Pyridone-Aminal eFT508 Targeting Dysregulated Translation by Selective Mitogen-activated Protein Kinase Interacting Kinases 1 and 2 (MNK1/2) Inhibition. *J. Med. Chem.* **2018**, *61*, 3516−3540.
(31) Santag, S.; Siegel, F.; Wengner, A. M.; Lange, C.; Bomer, U.; Eis, K.; Puhler, F.; Lienau, P.; Bergemann, L.; Michels, M.; von Nussbaum, F.; Mumberg, D.; Petersen, K. BAY 1143269, a novel MNK1 inhibitor, targets oncogenic protein expression and shows potent anti-tumor activity. *Cancer Lett.* **2017**, *390*, 21−29.
(32) Yang, H.; Chennamaneni, L. R.; Ho, M. W. T.; Ang, S. H.; Tan, E. S. W.; Jeyaraj, D. A.; Yeap, Y. S.; Liu, B.; Ong, E. H.; Joy, J. K.; Wee, J. L. K.; Kwek, P.; Retna, P.; Dinie, N.; Nguyen, T. T. H.; Tai, S. J.; Manoharan, V.; Pendharkar, V.; Low, C. B.; Chew, Y. S.; Vuddagiri, S.; Sangthongpitag, K.; Choong, M. L.; Lee, M. A.; Kannan, S.; Verma, C. S.; Poulsen, A.; Lim, S.; Chuah, C.; Ong, T. S.; Hill, J.; Matter, A.; Nacro, K. Optimization of Selective Mitogen-Activated Protein Kinase Interacting Kinases 1 and 2 Inhibitors for the Treatment of Blast Crisis Leukemia. *J. Med. Chem.* **2018**, *61*, 4348−4369.
(33) Jin, X.; Merrett, J.; Tong, S.; Flower, B.; Xie, J.; Yu, R.; Tian, S.; Gao, L.; Zhao, J.; Wang, X.; Jiang, T.; Proud, C. G. Design, synthesis and activity of Mnk1 and Mnk2 selective inhibitors containing thieno[2,3-d]pyrimidine scaffold. *Eur. J. Med. Chem.* **2019**, *162*, 735−751.
(34) Jin, X.; Yu, R.; Wang, X.; Proud, C. G.; Jiang, T. Progress in developing MNK inhibitors. *Eur. J. Med. Chem.* **2021**, *219*, No. 113420.
(35) Hantschel, O. Unexpected off-targets and paradoxical pathway activation by kinase inhibitors. *ACS Chem. Biol.* **2015**, *10*, 234−245.
(36) Frye, S. V.; Johnson, G. L. Inhibitors paradoxically prime kinases. *Nat. Chem. Biol.* **2009**, *5*, 448−449.
(37) Cook, S. J.; Tucker, J. A.; Lochhead, P. A. Small molecule ERK5 kinase inhibitors paradoxically activate ERK5 signalling: be careful what you wish for. *Biochem. Soc. Trans.* **2020**, *48*, 1859−1875.
(38) Diab, S.; Teo, T.; Kumarasiri, M.; Li, P.; Yu, M.; Lam, F.; Basnet, S. K.; Sykes, M. J.; Albrecht, H.; Milne, R.; Wang, S. Discovery of 5-(2-(phenylamino)pyrimidin-4-yl)thiazol-2(3H)-one derivatives as potent Mnk2 inhibitors: synthesis, SAR analysis and biological evaluation. *ChemMedChem* **2014**, *9*, 962−972.
(39) Yu, M.; Li, P.; Basnet, S. K.; Kumarasiri, M.; Diab, S.; Teo, T.; Albrecht, H.; Wang, S. Discovery of 4-(dihydropyridinon-3-yl)amino-5-methylthieno[2,3-d]pyrimidine derivatives as potent Mnk inhibitors: synthesis, structure-activity relationship analysis and biological evaluation. *Eur. J. Med. Chem.* **2015**, *95*, 116−126.
(40) Bou-Petit, E.; Picas, E.; Puigjaner, C.; Font-Bardia, M.; Ferrer, N.; Sempere, J.; Puig de la Bellacasa, R.; Batllori, X.; Teixidó, J.; Estrada-Tejedor, R.; Ramon y Cajal, S.; Borrell, J. I. An unequivocal synthesis of 2-Aryl substituted 3-Amino-2,4,5,7-tetrahydro-6H-pyrazolo[3,4-b]pyridin-6-ones. *ChemistrySelect* **2017**, *2*, 3668−3672.
(41) Bou-Petit, E.; Plans, A.; Rodriguez-Picazo, N.; Torres-Coll, A.; Puigjaner, C.; Font-Bardia, M.; Teixido, J.; Ramon, Y. C. S.; Estrada-Tejedor, R.; Borrell, J. I. C4-C5 fused pyrazol-3-amines: when the degree of unsaturation and electronic characteristics of the fused ring controls regioselectivity in Ullmann and acylation reactions. *Org. Biomol. Chem.* **2020**, *18*, 5145−5156.
(42) Pettus, L. H.; Wurz, R. P.; Xu, S.; Herberich, B.; Henkle, B.; Liu, Q.; McBride, H. J.; Mu, S.; Plant, M. H.; Saris, C. J.; Sherman, L.;

https://doi.org/10.1021/acs.jmedchem.1c01941
J. Med. Chem. 2022, 65, 6070−6087

Wong, L. M.; Chmait, S.; Lee, M. R.; Mohr, C.; Hsieh, F.; Tasker, A. S. Discovery and evaluation of 7-alkyl-1,5-bis-aryl-pyrazolopyridinones as highly potent, selective, and orally efficacious inhibitors of p38alpha mitogen-activated protein kinase. *J. Med. Chem.* **2010**, *53*, 2973−2985.
(43) Camarasa, M.; Puig de la Bellacasa, R.; Gonzalez, A. L.; Ondono, R.; Estrada, R.; Franco, S.; Badia, R.; Este, J.; Martinez, M. A.; Teixido, J.; Clotet, B.; Borrell, J. I. Design, synthesis and biological evaluation of pyrido[2,3-d]pyrimidin-7-(8H)-ones as HCV inhibitors. *Eur. J. Med. Chem.* **2016**, *115*, 463−483.
(44) Falcó, J. L.; Lloveras, M.; Buira, I.; Teixido, J.; Borrell, J. I.; Mendez, E.; Terencio, J.; Palomer, A.; Guglietta, A. Design, synthesis and biological activity of acyl substituted 3-amino-5-methyl-1,4,5,7-tetrahydropyrazolo[3,4-b]pyridin-6-ones as potential hypnotic drugs. *Eur. J. Med. Chem.* **2005**, *40*, 1179−1187.
(45) Balsas, P.; Esteve-Arenys, A.; Roldan, J.; Jimenez, L.; Rodriguez, V.; Valero, J. G.; Chamorro-Jorganes, A.; de la Bellacasa, R. P.; Teixido, J.; Matas-Cespedes, A.; Moros, A.; Martinez, A.; Campo, E.; Saez-Borderias, A.; Borrell, J. I.; Perez-Galan, P.; Colomer, D.; Roue, G. Activity of the novel BCR kinase inhibitor IQS019 in preclinical models of B-cell non-Hodgkin lymphoma. *J. Hematol. Oncol.* **2017**, *10*, No. 80.
(46) Lavecchia, M. J.; Puig de la Bellacasa, R.; Borrell, J. I.; Cavasotto, C. N. Investigating molecular dynamics-guided lead optimization of EGFR inhibitors. *Bioorg. Med. Chem.* **2016**, *24*, 768−778.
(47) Ueda, T.; Watanabe-Fukunaga, R.; Fukuyama, H.; Nagata, S.; Fukunaga, R. Mnk2 and Mnk1 are essential for constitutive and inducible phosphorylation of eukaryotic initiation factor 4E but not for cell growth or development. *Mol. Cell. Biol.* **2004**, *24*, 6539−6549.
(48) Furic, L.; Rong, L.; Larsson, O.; Koumakpayi, I. H.; Yoshida, K.; Brueschke, A.; Petroulakis, E.; Robichaud, N.; Pollak, M.; Gaboury, L. A.; Pandolfi, P. P.; Saad, F.; Sonenberg, N. eIF4E phosphorylation promotes tumorigenesis and is associated with prostate cancer progression. *Proc. Natl. Acad. Sci. U.S.A.* **2010**, *107*, 14134−14139.
(49) Ueda, T.; Sasaki, M.; Elia, A. J.; Chio, I. I.; Hamada, K.; Fukunaga, R.; Mak, T. W. Combined deficiency for MAP kinase-interacting kinase 1 and 2 (Mnk1 and Mnk2) delays tumor development. *Proc. Natl. Acad. Sci. U.S.A.* **2010**, *107*, 13984−13990.
(50) Ke, X. Y.; Chen, Y.; Tham, V. Y.; Lin, R. Y.; Dakle, P.; Nacro, K.; Puhaindran, M. E.; Houghton, P.; Pang, A.; Lee, V. K.; Ding, L. W.; Gery, S.; Hill, J.; Chen, L.; Xu, L.; Koeffler, H. P. MNK1 and MNK2 enforce expression of E2F1, FOXM1, and WEE1 to drive soft tissue sarcoma. *Oncogene* **2021**, *40*, 1851−1867.
(51) Ramalingam, S.; Ramamurthy, V. P.; Gediya, L. K.; Murigi, F. N.; Purushottamachar, P.; Huang, W.; Choi, E. Y.; Zhang, Y.; Vasaitis, T. S.; Kane, M. A.; Lapidus, R. G.; Njar, V. C. O. The Novel Mnk1/2 Degrader and Apoptosis Inducer VNLG-152 Potently Inhibits TNBC Tumor Growth and Metastasis. *Cancers* **2019**, *11*, 299.
(52) Roskoski, R., Jr. Classification of small molecule protein kinase inhibitors based upon the structures of their drug-enzyme complexes. *Pharmacol. Res.* **2016**, *103*, 26−48.
(53) O'Loghlen, A.; Gonzalez, V. M.; Jurado, T.; Salinas, M.; Martin, M. E. Characterization of the activity of human MAP kinase-interacting kinase Mnk1b. *Biochim. Biophys. Acta, Mol. Cell Res.* **2007**, *1773*, 1416−1427.
(54) Shveygert, M.; Kaiser, C.; Bradrick, S. S.; Gromeier, M. Regulation of eukaryotic initiation factor 4E (eIF4E) phosphorylation by mitogen-activated protein kinase occurs through modulation of Mnk1-eIF4G interaction. *Mol. Cell. Biol.* **2010**, *30*, 5160−5167.
(55) Kung, J. E.; Jura, N. Structural Basis for the Non-catalytic Functions of Protein Kinases. *Structure* **2016**, *24*, 7−24.
(56) Attwood, M. M.; Fabbro, D.; Sokolov, A. V.; Knapp, S.; Schioth, H. B. Trends in kinase drug discovery: targets, indications and inhibitor design. *Nat. Rev. Drug Discovery* **2021**, *20*, 798.
(57) Ayala-Aguilera, C. C.; Valero, T.; Lorente-Macias, A.; Baillache, D. J.; Croke, S.; Unciti-Broceta, A. Small Molecule Kinase Inhibitor Drugs (1995-2021): Medical Indication, Pharmacology, and Synthesis. *J. Med. Chem.* **2021**, *65*, 1047−1131.
(58) Wu, P.; Nielsen, T. E.; Clausen, M. H. FDA-approved small-molecule kinase inhibitors. *Trends Pharmacol. Sci.* **2015**, *36*, 422−439.
(59) Okuzumi, T.; Fiedler, D.; Zhang, C.; Gray, D. C.; Aizenstein, B.; Hoffman, R.; Shokat, K. M. Inhibitor hijacking of Akt activation. *Nat. Chem. Biol.* **2009**, *5*, 484−493.
(60) Poulikakos, P. I.; Zhang, C.; Bollag, G.; Shokat, K. M.; Rosen, N. RAF inhibitors transactivate RAF dimers and ERK signalling in cells with wild-type BRAF. *Nature* **2010**, *464*, 427−430.
(61) Hatzivassiliou, G.; Song, K.; Yen, I.; Brandhuber, B. J.; Anderson, D. J.; Alvarado, R.; Ludlam, M. J.; Stokoe, D.; Gloor, S. L.; Vigers, G.; Morales, T.; Aliagas, I.; Liu, B.; Sideris, S.; Hoeflich, K. P.; Jaiswal, B. S.; Seshagiri, S.; Koeppen, H.; Belvin, M.; Friedman, L. S.; Malek, S. RAF inhibitors prime wild-type RAF to activate the MAPK pathway and enhance growth. *Nature* **2010**, *464*, 431−435.
(62) Chan, T. O.; Zhang, J.; Rodeck, U.; Pascal, J. M.; Armen, R. S.; Spring, M.; Dumitru, C. D.; Myers, V.; Li, X.; Cheung, J. Y.; Feldman, A. M. Resistance of Akt kinases to dephosphorylation through ATP-dependent conformational plasticity. *Proc. Natl. Acad. Sci. U.S.A.* **2011**, *108*, E1120−E1127.
(63) Cameron, A. J. M.; Escribano, C.; Saurin, A. T.; Kostelecky, B.; Parker, P. J. PKC maturation is promoted by nucleotide pocket occupation independently of intrinsic kinase activity. *Nat. Struct. Mol. Biol.* **2009**, *16*, 624−630.
(64) Kunkel, M. T.; Newton, A. C. Protein kinase d inhibitors uncouple phosphorylation from activity by promoting agonist-dependent activation loop phosphorylation. *Chem. Biol.* **2015**, *22*, 98−106.
(65) Ross, F. A.; Hawley, S. A.; Auciello, F. R.; Gowans, G. J.; Atrih, A.; Lamont, D. J.; Hardie, D. G. Mechanisms of Paradoxical Activation of AMPK by the Kinase Inhibitors SU6656 and Sorafenib. *Cell Chem. Biol.* **2017**, *24*, 813−824.
(66) Higuchi, M.; Ishiyama, K.; Maruoka, M.; Kanamori, R.; Takaori-Kondo, A.; Watanabe, N. Paradoxical activation of c-Src as a drug-resistant mechanism. *Cell Rep.* **2021**, *34*, No. 108876.
(67) Lochhead, P. A.; Tucker, J. A.; Tatum, N. J.; Wang, J.; Oxley, D.; Kidger, A. M.; Johnson, V. P.; Cassidy, M. A.; Gray, N. S.; Noble, M. E. M.; Cook, S. J. Paradoxical activation of the protein kinase-transcription factor ERK5 by ERK5 kinase inhibitors. *Nat. Commun.* **2020**, *11*, No. 1383.
(68) Tong, M.; Seeliger, M. A. Targeting conformational plasticity of protein kinases. *ACS Chem. Biol.* **2015**, *10*, 190−200.
(69) Ryckaert, J.-P.; Ciccotti, G.; Berendsen, H. J. C. Numerical integration of the cartesian equations of motion of a system with constraints: molecular dynamics of n-alkanes. *J. Comput. Phys.* **1977**, *23*, 327−341.
(70) Darden, T.; York, D.; Pedersen, L. Particle mesh Ewald: AnN·log(N) method for Ewald sums in large systems. *J. Chem. Phys.* **1993**, *98*, 10089−10092.
(71) Homeyer, N.; Horn, A. H.; Lanig, H.; Sticht, H. AMBER force-field parameters for phosphorylated amino acids in different protonation states: phosphoserine, phosphothreonine, phosphotyrosine, and phosphohistidine. *J. Mol. Model.* **2006**, *12*, 281−289.
(72) Roe, D. R.; Cheatham, T. E., 3rd. PTRAJ and CPPTRAJ: Software for Processing and Analysis of Molecular Dynamics Trajectory Data. *J. Chem. Theory Comput.* **2013**, *9*, 3084−3095.
(73) Zhang, J. H.; Chung, T. D.; Oldenburg, K. R. A Simple Statistical Parameter for Use in Evaluation and Validation of High Throughput Screening Assays. *J. Biomol. Screening* **1999**, *4*, 67−73.
(74) Iversen, P. W.; Eastwood, B. J.; Sittampalam, G. S.; Cox, K. L. A comparison of assay performance measures in screening assays: signal window, Z′ factor, and assay variability ratio. *J. Biomol. Screening* **2006**, *11*, 247−252.
(75) Orellana, E. A.; Kasinski, A. L. Sulforhodamine B (SRB) Assay in Cell Culture to Investigate Cell Proliferation. *Bio-Protoc.* **2016**, *6*, No. e1984.

https://doi.org/10.1021/acs.jmedchem.1c01941
J. Med. Chem. 2022, 65, 6070−6087